Chapter 1
Introduction

The U.S. National Aeronautics and Space Administration (NASA) Deep Space Network (DSN) is the largest and most sensitive scientific telecommunications and radio navigation network in the world. Its principal responsibilities are to support radio and radar astronomy observations in the exploration of the solar system and the universe. The network consists of three deep-space communications complexes (DSCCs), which are located on three continents: at Goldstone, in Southern California's Mojave Desert; near Madrid, Spain; and near Canberra, Australia. Each of the three complexes consists of multiple deep-space stations equipped with ultrasensitive receiving systems and large parabolic dish antennas. At each complex, there are multiple 34-m-diameter antennas, one 26-m antenna, one 11-m antenna, and one 70-m antenna. A centralized signal processing center (SPC) remotely controls the 34- and 70-m antennas, generates and transmits spacecraft commands, and receives and processes spacecraft telemetry.

The main features of the complex are the large parabolic dish antennas and their support structures. Although their diameters and mountings differ, all antennas employ a Cassegrain-type feed system that is essentially the same as that of a Cassegrain telescope, used in optical astronomy. Each antenna dish surface is constructed of precision-shaped perforated aluminum panels of specified surface accuracy, secured to an open steel framework.

This monograph details the evolution of the large parabolic dish antennas from the initial 26-m operation at L-band (960 MHz) in 1958 through the present Ka-band (32-GHz) operation on the 70-m antenna and provides a rather complete history of the DSN antennas. Design, performance analysis, and measurement techniques are highlighted. Sufficient information is provided to

allow the sophisticated antenna professional to replicate the radio frequency optics designs.

The first DSN antenna began operating in November 1958 and was initially used to support Pioneers 3 and 4. The antenna site was subsequently named the Pioneer Deep Space Station. It began operation with a focal-point feed system but was quickly converted to a Cassegrain configuration, which remained until the antenna was decommissioned in 1981. In 1985, the U.S. National Park Service declared the site a national historic landmark.

The present Echo antenna, originally 26 m in diameter, was erected in late 1962 and was extended to 34 m in 1979. Both the Pioneer and Echo antennas were patterned after radio-astronomy antennas then in use at the Carnegie Institution of Washington (D.C.) and the University of Michigan. The main features borrowed from the radio-astronomy antenna design were the mount and the celestial-coordinate pointing system.

The Venus site began operation in 1962 as the Deep Space Network research and development (R&D) station and has remained the primary R&D site for DSN antennas. Almost all technological innovations in DSN antennas have first been tested at this site. The original 26-m antenna was equipped with an azimuth–elevation-type mount that could operate at 2 deg/s in azimuth and elevation. This antenna is no longer in use, replaced in 1990 by the first beam-waveguide (BWG) antenna.

The first 64-m antenna was completed in 1966 and was a physical scale-up of the 26-m antenna. Initial operation was at S-band (2.110–2.120 GHz transmit and 2.27–2.30 GHz receive). In 1968, an X-band feed cone was installed. A feed cone is a sheet-metal conical shell that houses the feed horn, low-noise amplifiers, and ancillary equipment. As the need developed for changing feed cones rapidly, the standard feed-cone support structure was replaced with a structure capable of supporting three fixed feed cones. In addition, the subreflector was modified to permit rapid changing of feed cones by rotating an asymmetrically truncated subreflector about its symmetric axis and pointing it toward the feed. Simultaneous multifrequency was provided by a reflex–dichroic feed system. In support of the NASA Voyager spacecraft encounter at Neptune in 1989, additional performance was realized by increasing the size of the antenna to 70 m, using dual-shaped optics, and improving the main-reflector surface accuracy through the use of high-precision panels. During the 1990s, the potential use of Ka-band on the 70-m antenna was demonstrated through R&D experiments, and in June 2000, X-band (7.145–7.190 GHz) uplink capability was added.

In 1982, a new design for a 34-m antenna with a common-aperture feed horn as well as dual-shaped optics designed for optimum gain over noise temperature (G/T) was introduced into the DSN and designated the high-efficiency (HEF) antenna. There is now one HEF at every DSCC.

Early in 1990, a new R&D antenna was fabricated and tested as a precursor to introducing BWG antennas and Ka-band frequencies into the DSN. The R&D antenna was initially designed for X- and Ka-bands but was subsequently upgraded to include S-band. Based upon the knowledge gained with this antenna, operational BWG antennas were included in the network. There are three 34-m BWG antennas at Goldstone, one in Spain, and one in Australia, with one under construction (as of 2002) in Spain and a second planned for Australia.

Also in the 1990s, two BWG antennas capable of supporting X-band high power were built and tested. As they were only a technology demonstration, their original design was never introduced into the network. Rather, one of the two was retrofitted for S-band support and is still in use in that capacity.

This monograph will trace the history of DSN large-antenna technology through the development and implementation of the antennas at the Goldstone complex, since, with the exception of the 64-to-70-m upgrade, the technology improvements were first introduced there. Chapter 1 presents the methods of analysis, with supporting mathematical details, and measurement and design techniques for reflector antennas. Chapters 2 through 9 cover each type of antenna, and Chapter 10 explores current thinking.

1.1 Technology Drivers

The prime mission of the DSN is to receive extremely weak signals over vast interplanetary distances. A key element of the telecommunications-link performance is the received power signal-to-noise ratio (SNR), which is given by

$$S/N = \frac{P_T G_T A_R}{4\pi R^2 N} = \frac{P_T G_T G_R}{kBT_S(4\pi R/\lambda)^2} \tag{1.1-1}$$

where

P_T = spacecraft transmit power
G_T = transmit gain
G_R = receive gain
R = distance to the spacecraft
N = total noise
A_T = the effective area of the transmit (spacecraft) antenna
A_R = the effective areas of the receive ground antennas
T_s = receive system-noise temperature
λ = wavelength

k = Boltzman's constant

B = bandwidth.

To do its part effectively, the ground antenna system must maximize the ratio of received signal to the receiving system noise power, which is measured by an antenna figure of merit (FM), defined as the ratio of antenna effective area (or equivalently gain) to system-noise temperature.

The receive temperature consists primarily of the antenna feed system and amplifier contributions. For assessing the antenna FM, it is desirable to draw an imaginary reference plane between the receiver system and the antenna system, thus placing all noise contributions in one of these categories. If the receiver contribution (including the feed-system losses) is given by T_R and the antenna noise contribution by T_A, then the FM will be given by

$$FM = \frac{G_R}{T_R + T_A} \tag{1.1-2}$$

It can be readily seen that the antenna noise-temperature properties are very significant contributors to the FM, especially for the cases of low receiver noise-temperature systems. Also, the significant effect of total system-noise temperature on the FM is apparent. Thus, to maximize the FM for a given antenna size and frequency of operation, it is necessary to both maximize the antenna gain and minimize the total system-noise temperature. Since the individual contributions to noise temperature are additive and essentially independent of each other, it is necessary to individually minimize each contribution. If any one of the noise contributions is large, minimizing the others only marginally improves the FM. However, by using cryogenic amplifiers, the receiver noise-temperature contribution can be small (as low as 2 to 3 K for the highest-performing masers), and it then becomes imperative to minimize both the antenna and feed-system contributions. For ambient conditions, it should be noted that feed-system losses contribute to noise temperature at the rate of 7 K per 0.1-dB loss.

Techniques for maximizing the antenna gain and aperture efficiency of reflector antennas involve control of the illumination function. By definition, a feed system, which uniformly illuminates the antenna aperture with the proper polarization and has no spillover energy or other losses, possesses 100 percent aperture efficiency. In practice, however, some spillover is present due to the finite size of the feed illuminating a single reflector system or the subreflector illuminating the main reflector of a dual reflector system. One key result of this spillover is a thermal-noise contribution from the physically hot ground. Clearly, then, an ideal feed system has a very rapid energy cutoff at the reflector

edge, thereby maintaining relatively uniform reflector illumination while at the same time minimizing spillover energy.

Many design principles for large reflector antennas are borrowed from those successfully used in designing optical telescopes. For example, the earliest antenna design used a two-reflector Cassegrain system in which the main reflector was a paraboloid and the subreflector a hyperboloid. Subsequent designs incorporated dual-shaped optics, which offer higher efficiency for the same-size aperture. Although not as yet used in the DSN (as of 2002), clear-aperture designs (in which the radiating aperture is not blocked by either the subreflector or subreflector supports) offer the potential for even higher efficiencies.

Surface accuracy is also an important parameter in determining effective aperture area, as is demonstrated in Fig. 1-1, which plots the reduction in gain versus root-mean-square (rms) surface error. It demonstrates that the rms surface error must be an extremely small fraction of the reflector diameter.

Surface errors fall into two main categories: (a) time-invariant panel mechanical manufacturing errors and panel-setting errors at the rigging angle and (b) time-varying errors induced by gravity, wind, and thermal effects. Improvements in panel manufacturing and in panel setting using microwave holography have left gravity distortions as a function of elevation angles as the major error source in DSN antennas for higher-frequency operation.

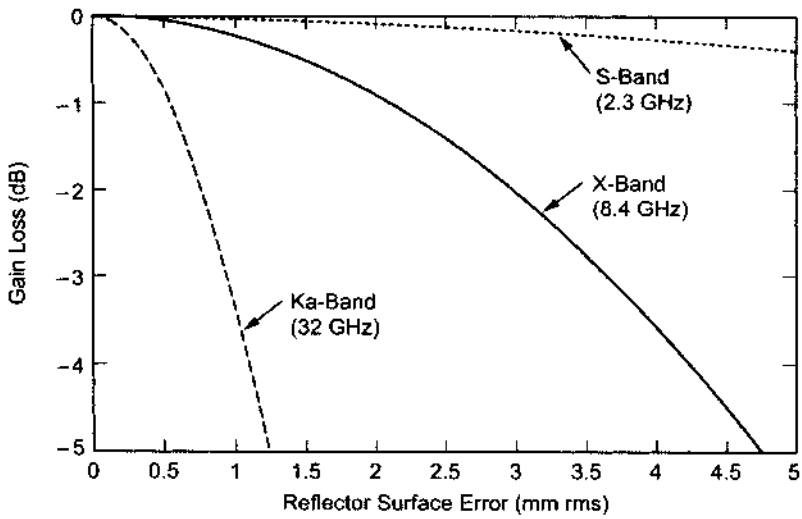

Fig. 1-1. Gain loss due to reflector surface error.

1.1.1 Frequency Bands Allocated to the Deep Space Network

Frequency ranges have been allocated by the International Telecommunication Union (ITU) for use in deep-space and near-Earth research. These ranges are listed in Table 1-1.

Table 1-1. Allocated frequency bands (GHz).

Band	Deep-Space Bands for Spacecraft Farther Than 2 Million km from Earth		Near-Earth Bands for Spacecraft Closer Than 2 Million km from Earth	
	Uplink[a]	Downlink[b]	Uplink[a]	Downlink[b]
S	2.110–2.120	2.290–2.300	2.025–2.110	2.200–2.290
X	7.145–7.190	8.400–8.450	7.190–7.235	8.450–8.500
Ka	34.200–34.700	31.800–32.300	Not applicable	Not applicable

[a] Earth to space.
[b] Space to Earth.

1.2 Analysis Techniques for Designing Reflector Antennas

Reflector antennas have existed since the days of Heinrich Hertz. They are one of the best solutions to requirements for cost-effective, high-dB/kg, high-performance antenna systems.

For a large ground antenna, it is not feasible to build a scale model to verify a new design. Hence, extremely accurate design-analysis tools are required. Fortunately, physical optics (PO) provides the required performance-estimate accuracy. All of the DSN antennas were designed and analyzed using PO, and the measured performance is within a few percent of the calculated values.

In addition to PO, many other techniques are required to completely design and characterize an antenna system. For example, accurate programs to design and analyze the feed horn and transform far-field patterns to near-field patterns for use in the PO analysis are essential. Programs to determine the reflector shape for maximum gain, or *G/T*, are also used. And quasioptical techniques such as geometric optics (GO), Gaussian-beam analysis, and or ray tracing are useful for a quick characterization of BWG systems. Tools to design and analyze frequency-selective surfaces are needed for use in multifrequency systems. And since the FM for these antennas is *G/T*, accurate programs to predict noise performance are required.

The basic mathematical details of each of these techniques are given in this section, with examples of their use sprinkled throughout this monograph.

1.2.1 Radiation-Pattern Analysis

By far the most important analytical tool is physical optics, which is used to calculate the scattered field from a metallic reflecting surface—in this case, a reflector antenna. Electric currents, which excite the scattered field, are induced on the conducting surface by an incident wave assumed to be of a known amplitude, phase, and polarization everywhere in space (from a feed or other reflecting surface, for example). The PO approximations to the induced surface currents are valid when the reflector is smooth and the transverse dimensions are large in terms of wavelengths. The closed reflecting surface is divided into a region S_1, which is illuminated by direct rays from the source ("illuminated region") and a region S_2, which is geometrically shadowed ("shadowed region") from direct rays from the source (Fig. 1-2). The PO approximations for the induced surface current distribution are

$$\begin{aligned} J_s &= 2(\hat{n} \times H_{inc}) \quad \text{on } S_1 \\ J_s &= 0 \qquad\qquad\quad \text{on } S_2 \end{aligned} \tag{1.2-1}$$

where $\hat{n}$ is the surface normal and H_{inc} the incident field. The expressions are then inserted into the radiation integral [1] to compute the scattered field.

Rusch and Potter [2] provide a good introduction to the early techniques used for analyzing DSN reflector antennas. More recently, due primarily to the orders-of-magnitude improvements in computer speed and memory, a very simple but extremely robust algorithm has emerged as the computer program of choice for computing the PO radiation integral. Its initial limitation to small reflectors was primarily due to the speed and memory limitations of the then-existing computers. The algorithm is documented in [3] and [4], but because of its extreme importance and to provide a fairly complete reference, it is repeated here.

One of the simplest possible reflector-antenna computer programs is based on a discrete approximation of the radiation integral. This calculation replaces the actual reflector surface with a triangular facet representation so that the

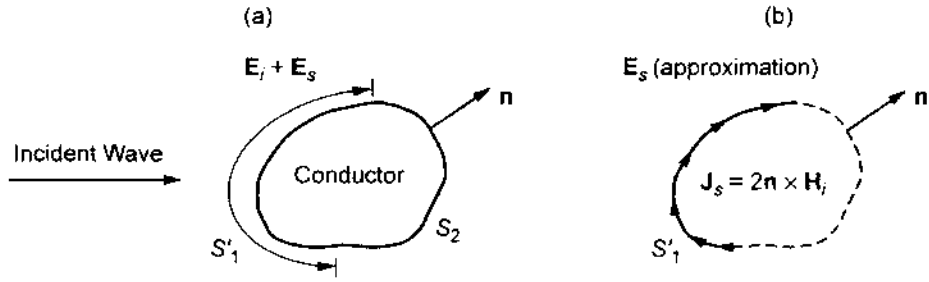

Fig. 1-2. The physical optics approximation: (a) original problem and (b) approximation.

reflector resembles a geodesic dome. The PO current is assumed to be constant in magnitude and phase over each facet, so the radiation integral is reduced to a simple summation. This program was originally developed in 1970 and has proven to be surprisingly robust and useful for the analysis of reflectors, particularly when the near field is desired and the surface derivatives are not known.

Two improvements significantly enhanced the usefulness of the computer programs: the first was the orders-of-magnitude increase, over time, in computer speed and memory and the second was the development of a more sophisticated approximation of the PO surface current, which permitted the use of larger facets. The latter improvement is due to the use of a linear-phase approximation of the surface current. Within each triangular region, the resulting integral is the 2-D Fourier transform of the projected triangle. This triangular-shape function integral can be computed in closed form. The complete PO integral is then a summation of these transforms.

1.2.1.1 Mathematical Details. The PO radiation integral over the reflector surface, Σ, can be expressed as [5]

$$\mathbf{H}(\mathbf{r}) = -\frac{1}{4\pi}\int_{\Sigma}\left(jk + \frac{1}{R}\right)\hat{\mathbf{R}} \times \mathbf{J}(\mathbf{r}')\frac{e^{-jkR}}{R}ds' \qquad (1.2\text{-}2)$$

in which

$\mathbf{r}$ = the field point
$\mathbf{r}'$ = source point
R = $|\mathbf{r} - \mathbf{r}'|$ is the distance between them
$\hat{\mathbf{R}}$ = $(\mathbf{r} - \mathbf{r}')/R$ is a unit vector
$\mathbf{J}(\mathbf{r}')$ = the surface current
λ = wavelength
k = $2\pi/\lambda$.

For the purpose of analysis, the true surface, Σ, is replaced by a contiguous set of triangular facets. These facets, denoted Δ_i, are chosen to be roughly equal in size with their vertices on the surface, Σ. Fig. 1-3 shows a typical facet and its projection onto the x, y plane. Let (x_i, y_i, z_i) represent the centroid of each triangle where the subscript $i = 1, \cdots, N$ is associated with a triangle. Then, the field obtained by replacing the true surface, Σ, by the triangular facet approximation is

$$\mathbf{H}(\mathbf{r}) = -\frac{1}{4\pi}\sum_{i=1}^{N}\int_{\Delta_i}\left(jk + \frac{1}{R}\right)\hat{\mathbf{R}} \times \mathbf{J}(\mathbf{r}')\frac{e^{-jkR}}{R}ds' \qquad (1.2\text{-}3)$$

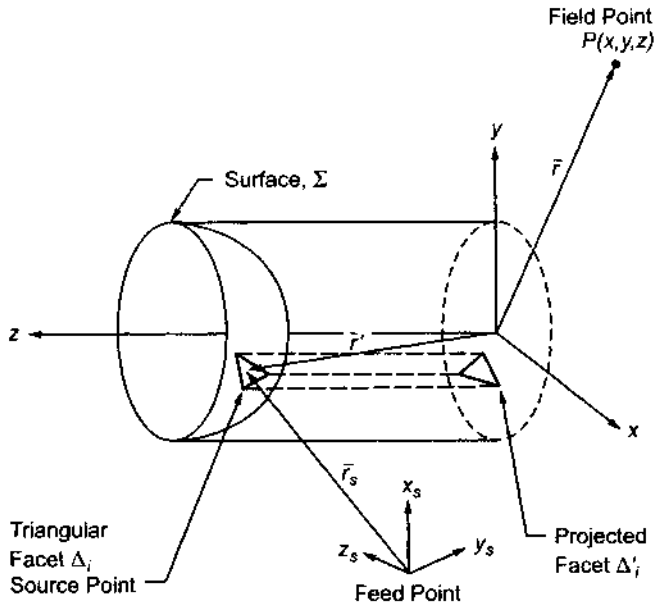

Fig. 1-3. Reflector-analysis coordinate systems and a typical triangular facet.

In Eq. (1.2-3), $\mathbf{J}$ is now the equivalent surface current evaluated on the triangular facets. Since the triangles are small, it is expected that $\hat{\mathbf{R}}$ and R do not vary appreciably over the area of a given facet. Thus, let $\hat{\mathbf{R}}_i$ and R_i be the value obtained at the centroid (x_i, y_i, z_i) of each facet and approximate Eq. (1.2-3) by

$$\mathbf{H}(\mathbf{r}) = -\frac{1}{4\pi} \sum_{i=1}^{N} \left[jk + \frac{1}{R_i} \right] \hat{\mathbf{R}}_i \times \mathbf{T}_i(\mathbf{r}) \tag{1.2-4}$$

$$\mathbf{T}_i(\mathbf{r}) = \int_{\Delta_i} \mathbf{J}_i(\mathbf{r}') \frac{e^{-jkR}}{R_i} ds' \tag{1.2-5}$$

Assume that the necessary transformations have been performed so that the incident field, $\mathbf{H}_s$, is given in terms of the reflector coordinate system. Then

$$\mathbf{J}_i(\mathbf{r}') = 2\hat{\mathbf{n}}_i \times \mathbf{H}_s(\mathbf{r}') \tag{1.2-6}$$

Next, assume that the incident field can be represented by a function of the form

$$\mathbf{H}_s = \mathbf{h}_s(\mathbf{r}_i) \frac{e^{-jkr_s}}{4\pi r_{si}} \tag{1.2-7}$$

where r_s is the distance to the source point and r_{si} is the distance from the triangle centroid to the source point. Then, Eq. (1.2-5) can be written

$$\mathbf{T}_i(\mathbf{r}) = \frac{\hat{n}_i \times \mathbf{h}_s(\mathbf{r}_i)}{2\pi R_i r_{si}} \int_{\Delta_i} e^{-jk(R+r_s)} ds' \tag{1.2-8}$$

Making use of the Jacobian and approximating

$$R(x,y) + r_s(x,y) = \frac{1}{k}\left(a_i - u_i x - v_i y\right) \tag{1.2-9}$$

in which a_i, u_i, and v_i are constants, the expression can be rewritten as

$$\mathbf{T}_i(\mathbf{r}) = \frac{\hat{\mathbf{n}}_i \times \mathbf{h}_s(\mathbf{r}_i)}{2\pi R_i r_{si}} J_{\Delta_i} e^{-jai} \int_{\Delta_i'} e^{j(u_i x' + v_i y')} dx'dy' \tag{1.2-10}$$

where the surface normal to the surface $z = f(x,y)$ is

$$\mathbf{N}_i = -\hat{\mathbf{x}} f_{xi} - \hat{\mathbf{y}} f_{yi} + \hat{\mathbf{z}} \tag{1.2-11}$$

where $f_x = \dfrac{\partial f}{\partial x}$ and the Jacobian is

$$J_{\Delta_i} = |\mathbf{N}_i| = \left[f_{xi}^2 + f_{yi}^2 + 1\right]^{1/2} \tag{1.2-12}$$

It may now be observed that this integral is the 2-D Fourier transform of the i^{th} projected triangle Δ_i', expressed as

$$S(u,v) = \int_{\Delta_i'} e^{j(ux' + vy')} dx'dy' \tag{1.2-13}$$

which can be computed in closed form as described in [6]. The full radiation integral is then the sum of all the transforms of the individual triangles.

1.2.1.2 Application to Dual-Reflector Antennas. The PO integration methodology is incorporated in a sequential fashion for the analysis of the dual-reflector antenna system. Initially, the feed illuminates the subreflector, and the currents on the subreflector surface are determined. Subsequently, the near fields scattered from the subreflector are used to illuminate the main reflector, and its induced currents are determined. The main reflector scattered fields are then determined by integrating these currents.

Many coordinate systems are required to allow flexibility in locating and orienting the feed, subreflector, main reflector, and output-pattern generation. The relation among the various coordinate systems is depicted in Fig. 1-4.

1.2.1.3 Useful Coordinate Transformations. In the discussion of the preceding sections (1.2.1 and 1.2.1.2), the analysis is performed using two distinct coordinate systems: reflector and feed coordinates. In addition, it is sometimes convenient to display the computed patterns in yet another coordinate system. Consequently, one must know the transformation equations that permit coordinates and vectors described in one coordinate system to be expressed in terms of some other coordinate system. The transformation may require both translation and rotation. The required transformations are described below. They are the Cartesian-to-spherical transformation and coordinate rotations using Eulerian angles.

The Cartesian-to-spherical transformation is conveniently summarized in matrix form. With the Cartesian components of a vector, **H**, denoted (H_x, H_y, H_z) and the spherical components (H_r, H_θ, H_ϕ), one finds that the transformation is

$$\begin{bmatrix} H_r \\ H_\theta \\ H_\phi \end{bmatrix} = \begin{bmatrix} \sin\theta\cos\phi & \sin\theta\sin\phi & \cos\theta \\ \cos\theta\cos\phi & \cos\theta\sin\phi & -\sin\theta \\ -\sin\phi & \cos\phi & 0 \end{bmatrix} \begin{bmatrix} H_x \\ H_y \\ H_z \end{bmatrix} \tag{1.2-14}$$

The inverse transformation is just the transpose of the above matrix.

Rotations are handled by the use of the Eulerian angles (α,β,γ). These angles describe three successive rotations that bring one Cartesian system

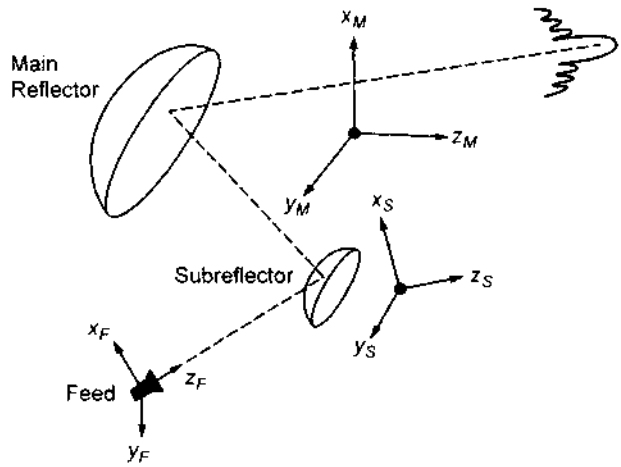

Fig. 1-4. Dual-reflector coordinate systems.

into alignment with another. Let the two systems be denoted (x_1, y_1, z_1) and (x_2, y_2, z_2). As illustrated in Fig. 1-5, the angles are defined as follows:

- α describes a positive rotation about the z_1-axis, which brings the x_1-axis into the x′-axis aligned with the *line of nodes* (the line of intersection between the (x_2, y_2) and (x_1, y_1) planes)
- β describes a positive rotation about the line of nodes (the x′-axis) that brings the z_1-axis to z_2
- γ describes a positive rotation about the z_2-axis, which brings the x′-axis to the x_2-axis.

The phrase "positive rotation" means the direction of increasing angular measure as defined by the right-hand rule with respect to the axis about which the rotation occurs. Each of the rotations just described is performed using the standard rotation of coordinate formulas of plane analytic geometry.

When these expressions are written in matrix form and applied successively as described above, one obtains the following matrix equation that represents a general 3-D rotation of coordinates:

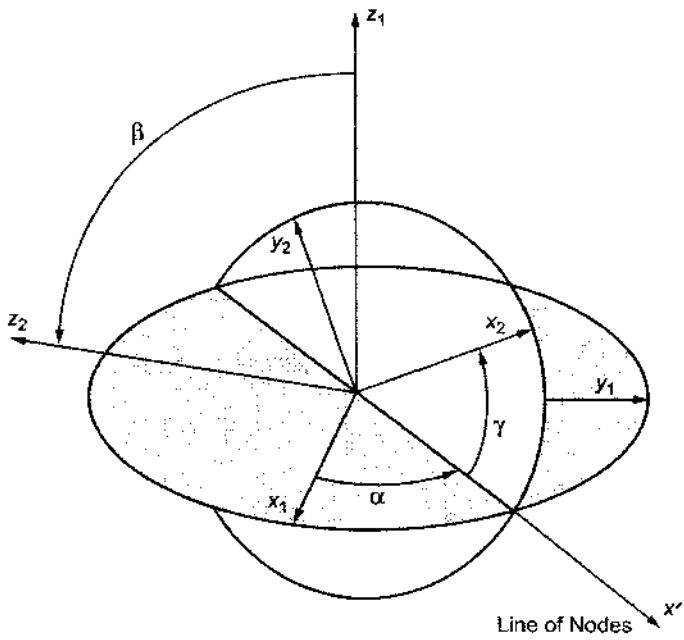

Fig. 1-5. Euler-angle definitions.

$$\begin{bmatrix} x_2 \\ y_2 \\ z_2 \end{bmatrix} = \begin{bmatrix} A_{11} & A_{12} & A_{13} \\ A_{21} & A_{22} & A_{23} \\ A_{31} & A_{32} & A_{33} \end{bmatrix} \begin{bmatrix} x_1 \\ y_1 \\ z_1 \end{bmatrix} \tag{1.2-15}$$

where the individual matrix elements are

$$A_{11} = \cos\gamma\cos\alpha - \sin\gamma\cos\beta\sin\alpha$$

$$A_{12} = \cos\gamma\cos\alpha + \sin\gamma\cos\beta\cos\alpha$$

$$A_{13} = \sin\gamma\sin\beta$$

$$A_{21} = -\sin\gamma\cos\alpha - \cos\gamma\cos\beta\sin\alpha$$

$$A_{22} = -\sin\gamma\cos\alpha + \cos\gamma\cos\beta\cos\alpha$$

$$A_{23} = \cos\gamma\sin\beta$$

$$A_{31} = \sin\beta\cos\gamma$$

$$A_{32} = -\sin\beta\cos\alpha$$

$$A_{33} = \cos\beta.$$

The inverse transformation is the transpose of the matrix given above.

Although the formulas are presented in terms of coordinate transformations, the transformation matrix is equally valid for the Cartesian components of a vector. Thus, the components of a vector, **H**, transform as

$$\begin{bmatrix} H_{x,2} \\ H_{y,2} \\ H_{z,2} \end{bmatrix} = \begin{bmatrix} A_{11} & A_{12} & A_{13} \\ A_{21} & A_{22} & A_{23} \\ A_{31} & A_{32} & A_{33} \end{bmatrix} \begin{bmatrix} H_{x,1} \\ H_{y,1} \\ H_{z,1} \end{bmatrix} \tag{1.2-16}$$

Further information can be found in [7].

1.2.1.4 A Numerical Example of Radiation-Pattern Analysis. In the 1980s, a FORTRAN program was written to perform the linear phase calculations indicated above. The program was extensively verified by comparing with measured data, for example, [8], and many other computer codes. A simple but interesting example is that of an ellipse, shown in Fig. 1-6.

The projected aperture of the ellipse is about 3 m. In the offset plane, centered on the x_p axis, the illumination function is a $\cos^{42}\theta$ pattern function (22.3-dB gain), and the frequency is 31.4 GHz. The ellipse is about 350λ along the major axis. Figure 1-7 compares the constant-phase approximation for three different grid densities: approximately 4000 and 10,000 and 23,000 triangles.

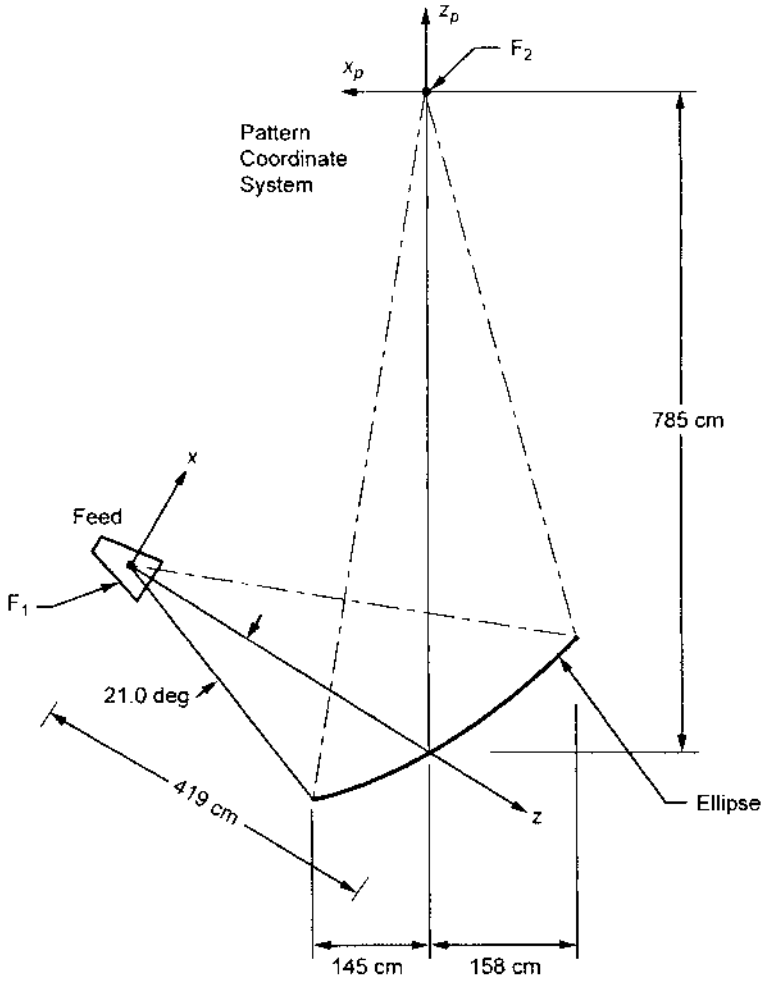

Fig. 1-6. Ellipse geometry.

This illustrates a general trend of the method; that is, depending on the size of the triangles, there is an angular limit over which the solution is valid. Figure 1-8 compares the linear-phase approximation with the constant-phase approximation for the 4000-triangle case and demonstrates that the angular range is larger with the linear-phase approximation.

1.2.2 Feed-Horn Analysis

An equally critical aspect of the analysis of reflector systems is the ability to accurately compute the radiation pattern of the feed. More details on the design of the feeds will be given later, but the analysis technique for computing the radiation patterns of the feed is summarized below.

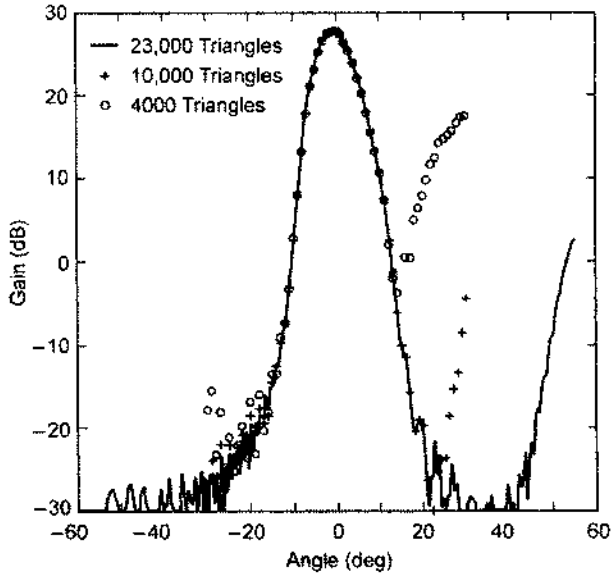

Fig. 1-7. Ellipse example: constant-phase approximation for offset plane.

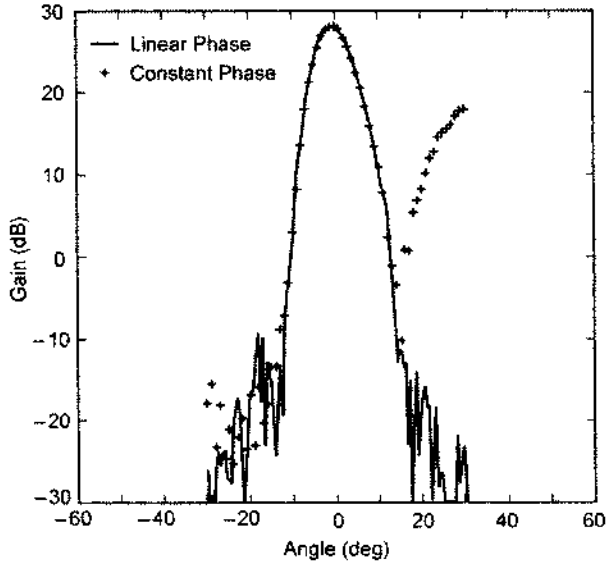

Fig. 1-8. Ellipse example: constant versus linear phase for offset plane.

Two types of feed horn possessing equal E- and H-plane patterns are commonly used. The first is the dual-mode feed horn [9], and the second is the corrugated feed horn [10]. In the dual-mode horn, a dominant-mode circular waveguide is connected to another guide of slightly larger diameter, where modes up to (transverse magnetic) TM_{11} may propagate, via a step transition. The step size is chosen to generate the precise amount of TM_{11} mode from the (transverse electric) TE_{11} mode so that when the two modes travel through the flared horn section that follows, the E- and H-plane patterns are equalized. The bandwidth of this feed horn is limited since the two modes must arrive at the horn aperture in phase, and the two modes have phase velocities that vary differently with frequency.

In the corrugated feed horn, the single-mode smooth-wall waveguide is connected to a corrugated waveguide that supports only the (hybrid) HE_{11} mode. Some matching between the waveguides is provided by gradually changing from $\lambda/2$ slot depth to $\lambda/4$ slot depth in a short transition region. Throughout the transition region, only the HE_{11} corrugated waveguide mode may propagate, and the E- and H-plane radiation patterns of this mode become nearly equal when the balanced condition is reached (slot depth = $\sim\lambda/4$). The bandwidth of this horn is larger than that of the dual-mode horn because the transverse electric field patterns and, hence, the radiation pattern of the HE_{11} mode are relatively insensitive to small changes in slot depth around the balanced condition (slot depth = $\sim\lambda/4$). After the HE_{11} mode is established in the single-mode corrugated waveguide, the guide is gradually flared, without changing the slot depth, to the required aperture size.

The corrugated section is analyzed using a computer code developed by Hoppe [11–13]. The analysis follows the method of James [14], expanding the fields inside each fin and slot in terms of circular waveguide modes, and matching the fields at each slot–fin boundary. All of the possible propagating modes as well as a sufficient number of evanescent modes are matched at each boundary, with results for successive edges and waveguide lengths cascading as the analysis moves through the device. In this way, the interaction between the fields of nonadjacent as well as adjacent slots are taken into account. The result of the calculation is a matrix equation relating the reflected and aperture modes to the input modes.

If $\mathbf{a}_1$ is a vector containing the power-normalized amplitudes of the input modes, then we may calculate the reflected modes, $\mathbf{b}_1$, and the aperture modes, $\mathbf{b}_2$, using

$$\mathbf{b}_2 = [S_{21}]\mathbf{a}_1 \tag{1.2-17}$$

$$\mathbf{b}_1 = [S_{11}]\mathbf{a}_1 \tag{1.2-18}$$

Here, $[S_{21}]$ and $[S_{22}]$ are the scattering matrices resulting from the computer run. (See the appendix of [14].) They depend only on frequency and device dimensions, not input modes. We may, therefore, specify any input vector $\mathbf{a}_1$ and calculate the reflected and aperture fields. Using the normalized amplitudes calculated above and the normalized vector functions giving the field distributions for each mode, we find the aperture field $\mathbf{E}_B$. The far field is then calculated by the method described by Silver and Ludwig [15,16].

$$\mathbf{E}_c = \frac{-1}{4\pi} \iint_S \left(-j\mu\omega\left(\hat{n} \times \mathbf{H}_B\right)\phi + \left(\hat{n} \times \mathbf{E}_B\right) \times \nabla\phi\right) ds \qquad (1.2\text{-}19)$$

where

μ = free-space permeability

ω = angular frequency $= 2\pi f$

$\hat{n}$ = unit vector normal to aperture surface

$\mathbf{H}_B$ = aperture magnetic field

ϕ = e^{-jkr}/r

$\mathbf{E}_B$ = aperture electric field

∇ = gradient operator

f = frequency

ds = incremented area on aperture surface

k = $2\pi/\lambda$

r = distance from the origin to the far-field point.

When $\mathbf{E}_B$ and $\mathbf{H}_B$ are represented in terms of circular waveguide modes, the resulting integrals have already been evaluated by Silver [16]. Therefore, given an input vector and the scattering matrix, we determine the aperture modes and composite far-field patterns. A spherical-wave analysis is then used to get the feed-horn near-field pattern for use in the PO software. Throughout the analysis, care must be taken to ensure proper normalization of the field amplitudes in terms of power. The smooth wall conical feed horn is modeled with the same software, only approximating the horn taper with small steps and zero-depth corrugated slots.

The mode-matching technique for analyzing corrugated horns yields excellent agreement with the measured patterns—so much so, in fact, that if the computed and measured patterns do not match, it is most likely due to measurement and/or manufacturing errors. A recent example of a fairly complicated horn is the X-/X-/Ka-band horn described in [17] and Chapter 9 of this mono-

graph. A comparison of the computed and measured patterns is shown in Figs. 1-9 and 1-10. This type of agreement is typical for a well-manufactured corrugated feed horn.

1.2.3 Spherical-Wave Analysis

Spherical-wave-expansion coefficients are normally used as one part of a sequence to analyze an antenna system. The basic role of the technique is to transform far-field patterns to the near-field H-field so that PO may be used for reflectors in the near field of their illumination source.

The theory of spherical waves is described in [18] and will only be briefly outlined here. Any electromagnetic field in a source-free region may be represented by a spherical-wave expansion. In general, the expansion must include both incoming and outgoing waves. If the field satisfies the radiation condition, only outgoing waves will be present, and the expansion will be valid outside the smallest sphere enclosing all sources (the sphere center must be at the coordinate origin used for the expansion). The radial dependence of the spherical waves is then given by the spherical Hankel function $h_n^2(kR)$. The second common case is an expansion valid inside the largest sphere enclosing no sources. In this case, the incoming and outgoing waves are present in equal amounts, producing a radial dependence given by the spherical Bessel function $j_n(kR)$.

Although the spherical-wave expansion can be applied to either of these two most common cases, the version used for the DSN assumes outgoing waves.

In either case, the input data that is used to specify the field is the tangential E-field on the surface of a sphere. For the first case, the data-sphere radius must be greater than or equal to the radius of the sphere enclosing the sources. For far-field data, the data-sphere radius is considered to be infinite. For the second case, the data-sphere radius must be less than or equal to the largest sphere enclosing no sources, and must be greater than zero.

The maximum value of the Hankel function index that is needed to closely approximate the field is roughly equal to ka (ka + 10 is typical, but in some cases a lower limit will work), where a is the radius of the sphere enclosing all (or no) sources for the first and second case, respectively.

Input data is specified on a grid of points defined by the intersection of constant contours of θ and ϕ. The amplitude and phase of E_θ and E_ϕ are given at each point. The minimum number of θ values is roughly 1.2 times the maximum value of n.

The azimuthal dependence of spherical waves is given by sin ($m\phi$) and cos ($m\phi$). In general, m runs from 0 to the maximum value of n. Frequently, symmetry can be used to reduce the number of azimuthal terms. A conical feed radiates only m = 1 modes, and reflection from a body of revolution will maintain this behavior. Secondly, there is an even and odd ϕ dependence, and fre-

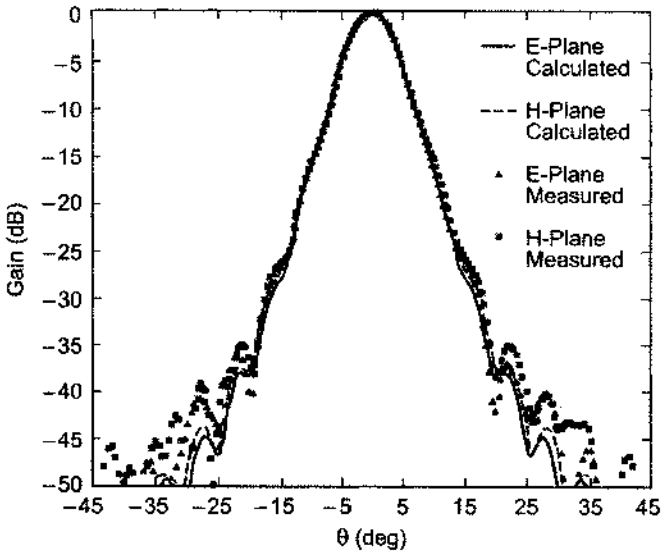

Fig. 1-9. Measured and computed patterns at 8.45 GHz (X-band receive) for the complete feed horn.

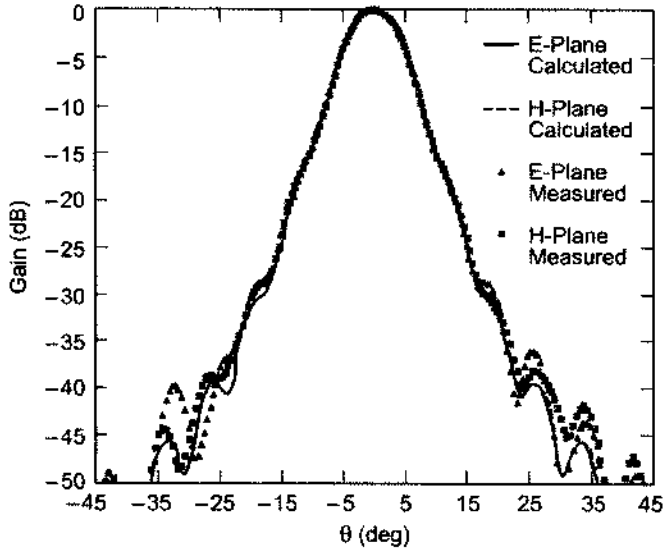

Fig. 1-10. Measured and computed patterns at 7.19 GHz (X-band transmit) for the complete feed horn.

quently, only one will be present. For the even case, E_θ can be expanded in only sin ($m\phi$) terms and E_ϕ in cos ($m\phi$) terms. For the odd case, this is reversed. The minimum number of ϕ values for the data sphere is, in general, $2M + 1$, where M is the maximum value of m. Symmetry can be used to reduce this value appropriately. The output of the computer program is the set of spherical-wave-expansion coefficients. These coefficients may then be used to compute the field anywhere within the region of validity. Therefore, the essential utility of the program is to take data consisting of the tangential E-field on a sphere (whose radius may be infinite) and provide the means of computing the field—all three components of E and H—at any other point in the region of validity.

The computer program used is patterned after that in [19].

1.2.4 Dual-Reflector Shaping

As initially used in the DSN, the Cassegrain reflector system had a parabolic main reflector and hyperbolic subreflector. The efficiency of these reflectors is primarily determined by (a) the ability of the feed system to illuminate only the reflectors while minimizing the energy that radiates elsewhere and (b) the ability of the feed to uniformly illuminate the parabola. Item (a), above, is termed "spillover efficiency" and (b) "illumination efficiency." The illumination efficiency is 100 percent when the energy density on the entire main reflector aperture is a constant.

Feed-horn patterns always taper gradually from their central maxima to nulls. If all this energy is intercepted by the reflector (for maximum spillover efficiency), the illumination is far from uniform, and the illumination efficiency is very poor. Consequently, any attempt to obtain nearly uniform illumination will result in a great loss of energy in spillover. Therefore, a compromise must be made. A common choice for both a prime focus system and the Cassegrain system is a 10-dB taper of the illumination pattern at the parabolic edge. This selection results in a combination of spillover and illumination efficiency of from about 75 to 80 percent.

It is possible, however, to change the shape of the two reflectors to alter the illumination function and improve efficiency. This methodology is termed dual-reflector shaping and was first introduced by Galindo [20], who demonstrated that one could design a dual-reflector antenna system to provide an arbitrary phase and amplitude distribution in the aperture of the main reflector. Thus, if one chose a uniform amplitude and constant phase, 100 percent illumination efficiency could be achieved. With the feed pattern given, the subreflector size would be chosen to give minimal spillover.

1.2.4.1 Theoretical Solution for the Symmetric Case. The complete solution can be found in [20] and [21] and only the uniform aperture case will be summarized below.

The geometry of the symmetric dual-reflector system is shown in Fig. 1-11. Due to circular symmetry, the synthesis reduces to the determination of the intersection curve (of the surface) with the plane through the axis of symmetry, that is, the x,y plane.

The synthesis method uses the analytical expressions of GO principles together with a geometry for the reflectors to develop a pair of first-order, nonlinear ordinary differential equations of the form

$$\frac{dy}{dx} = f(x,y) \tag{1.2-20}$$

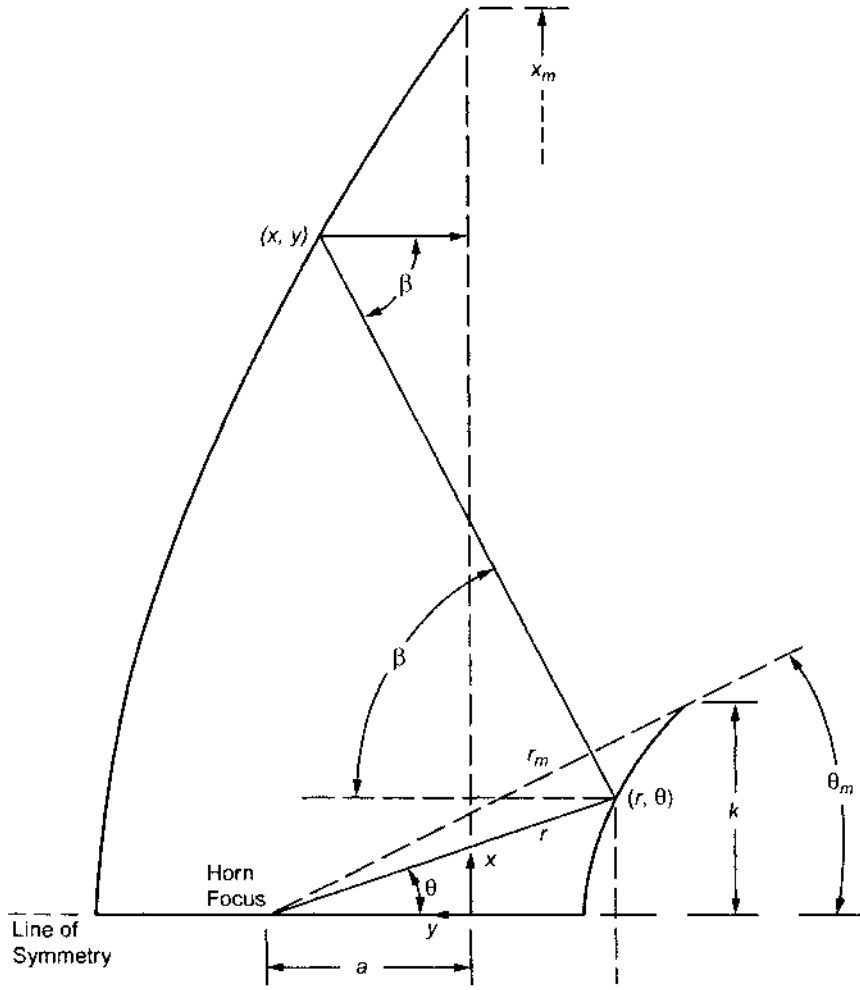

Fig. 1-11. Coordinate system for shaping.

which leads to cross sections of each reflector when subject to boundary conditions such as

$$y(x = x_{max}) = 0 \tag{1.2-21}$$

which are then solved by a high-speed digital computer.

The optical principles that are used to develop the required equations are that (a) the angle of incidence is equal to the angle of reflection (Snell's Law), (b) energy flow is conserved along the ray trajectories, and (c) surfaces of constant phase form normal surfaces to ray trajectories.

The incident field is assumed to have a spherical-phase function, that is, a phase center and a power-radiation pattern $F(\theta)$. For uniform phase in the aperture, the path length, $r + r' + r''$, must remain constant for all θ. Also, the amplitude function in the aperture $I(x)$ must also be equal to a prescribed distribution or a constant for maximum peak gain.

The equation for equal path lengths in the phase front is obtained from trigonometry:

$$r + y + \frac{x - r\sin\theta}{\sin\beta} = C \text{ (constant)} \tag{1.2-22}$$

where (x,y) and (r,θ) are the coordinates of points on the main reflector and subreflector, respectively.

The application of Snell's law to the two surfaces defines a relationship between the angles shown and the first derivates (slopes) of the surfaces. These are

$$\frac{1}{r}\frac{dr}{d\theta} = \tan\frac{\theta+\beta}{2} \tag{1.2-23}$$

$$\frac{-dy}{dx} = \tan\frac{\beta}{2} \tag{1.2-24}$$

Since the dual-reflector system is symmetrical about the y-axis, the total power within the increment $d\theta$ of the pattern $F(\theta)$ will be $F(\theta)2\pi \sin\theta d\theta$. Similarly, the total power within the increment dx of the main antenna aperture is $I(x)2\pi dx$, where $I(x)$ is the illumination function of the antenna aperture. Making $I(x)$ constant and equating the total power from $\theta = 0$ to angle θ to that within x, and normalizing by the total power, one obtains

$$x^2 = x_{max}^2 \frac{\int_0^{\theta} F(\theta)\sin\theta d\theta}{\int_0^{\theta_{max}} F(\theta)\sin\theta d\theta} \tag{1.2-25}$$

These four equations now have five dependent variables—x, y, r, θ, and β—and can be solved to provide equations for the surfaces.

Although the above procedure yields an optimum-gain antenna, the FM of a DSN antenna, as stated previously, is G/T. Dual-reflector shaping is based upon GO, but due to diffraction, the feed-horn energy scattered from the subreflector does not fall abruptly to zero at the edge of the main reflector. By choosing design parameters such that the geometric ray from the subreflector edge does not go all the way to the outer edge of the main reflector, it is possible to have the feed-horn energy at a very low level relative to the central region of the main reflector, which, in turn, results in the rear spillover noise contribution's becoming acceptably small. This procedure results in slightly lower illumination efficiency, but the significant reduction in noise from spillover also results in an optimum G/T ratio. The first antenna in the DSN to use dual-reflector shaping was the HEF antenna, the design of which is discussed in Chapter 6 of this monograph.

1.2.4.2 Offset-Shaped Reflector Antennas. The formulation shown in Section 1.2.4.1 (above) is for circularly symmetric reflector geometries. The exact solution has also been developed for offset geometries [22,23]. Offset geometry will have higher efficiency than symmetric geometry because the central blockage due to the subreflector can be eliminated. In the early 1980s, a 1.5-m antenna with an offset geometry was designed and built; it had an efficiency of 84.5 percent—the highest ever recorded [24]. However, due to the significantly greater mechanical complexity for an offset design, an offset-geometry antenna has never been incorporated into the DSN.

1.2.5 Quasioptical Techniques

Multiple reflector systems are typically analyzed by using PO, Gaussian beams, or ray-tracing techniques [25]. While PO offers high accuracy, it does so at the expense of computation time. This trade-off becomes particularly apparent in the analysis of multiple reflector antennas, such as BWG antennas, where PO is used to compute the currents on each reflector, based on the currents of the previous reflector. At the other end of the spectrum are ray tracing approaches that ignore diffraction effects entirely. These methods are fast but sacrifice the ability to accurately predict some effects such as cross-polarization.

More accurate than ray optics but less accurate than PO is Gaussian-beam analysis, which uses an appropriate set of expansion functions to model the field between the reflectors [26]. If the set is chosen wisely, only a few coefficients need to be determined from each reflector current. The field is then computed at the next reflector by using the expansion functions and their coefficients rather than by using the previous reflector current. For a BWG system with no enclosing tubes, an excellent set of expansion functions is the Gaussian-beam-mode set. In many cases, a preliminary design, which includes

diffraction effects, may be obtained by considering only the fundamental mode and a thin-lens model for the reflectors. Higher-order modes are included to model the effects of the curved reflector; these effects include asymmetric distortion of the beam, cross-polarization, and beam truncation.

1.2.5.1 PO Technique. The PO approach has been described in detail in Section 1.2.1 (above).

1.2.5.2 Gaussian-Beam Algorithm. In this section, the use of higher-order Gaussian beams to determine scattering by an arbitrary set of relectors is given. The geometry is depicted in Fig. 1-12. The steps for computing scattering are

1) Using PO, compute the current on the first reflector; the incident magnetic field is provided either by a feed model or by an incident set of Gaussian-beam modes
2) Using ray tracing, compute the direction of propagation for the reflected Gaussian-beam set; using a gut ray in the input direction specified by the feed coordinate system or by the input Gaussian-beam-set propagation

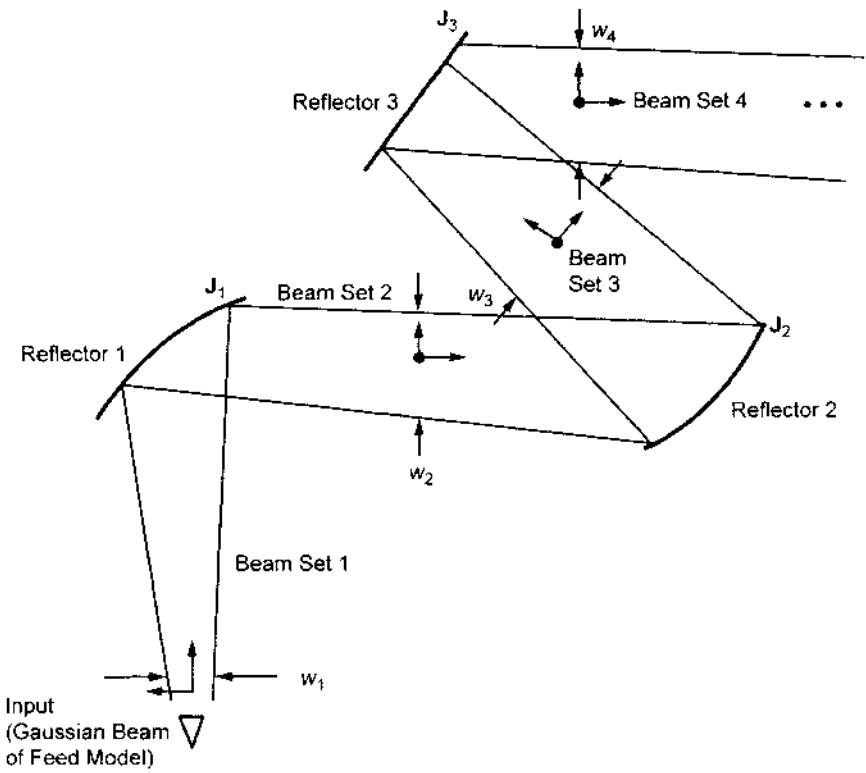

Fig. 1-12. Gaussian-beam geometry.

direction and the reflector surface description, compute the gut-ray direction for the output Gaussian-beam set

3) Determine the waist size and location for the output beam set

4) Determine the amplitudes of the individual modes in the output mode set

5) Repeat steps 1 to 4 for each additional reflector in the chain; in each of these cases, the previous Gaussian-beam set provides the input field for the current calculation

6) Using PO, compute the far-field pattern radiated by the final mirror.

One of the key steps in computing scattering of Gaussian-beam-mode sets by arbitrary reflector is the determination of the best choice for the output beam set's waist and its location. The problem is depicted in Fig. 1-13, where w_{in} and l_{in} are the input waist and location, and w_{out} and l_{out} are the same parameters for the output beam set. Once these parameters are determined, computation of the mode amplitudes from the current on the reflector follows easily. Proceed as follows:

1) Compute a waist at the reflector, denoted as w_{match}; when the input to the reflector is a Gaussian-beam-mode set, compute the input waist at the point of impact on the reflector; when the input to the reflector is a feed horn, determine an estimate of the waist from the reflector current (the output beam set is required to produce a waist equal to w_{match} at the point of impact; completing this step results in one of the two equations needed to compute the output beam-set parameters)

2) Next, derive a suitable set of points on the reflector to use for field matching or path-length matching (these points are generally chosen from within the waist at the point of impact)

3) Compute a phase center location for the input fields (for a Gaussian-beam-mode set, this is determined from the input radius of curvature at the point of impact; for a feed input, assume the phase center to be at the origin of the feed coordinate system)

4) Using the set of points on the reflector, compute the set of path lengths from the input phase center at each point, as shown in Fig. 1-13

5) Search for the output phase center (output radius of curvature), sweeping along the direction of the output ray (a minimum in the spread of the total path lengths from input phase center to reflector and then to output phase center is sought; generally, a single minimum is found either in front of or behind the reflector)

6) Using the output radius of curvature and the determined waist at the reflector, compute the waist size and location of the output beam set.

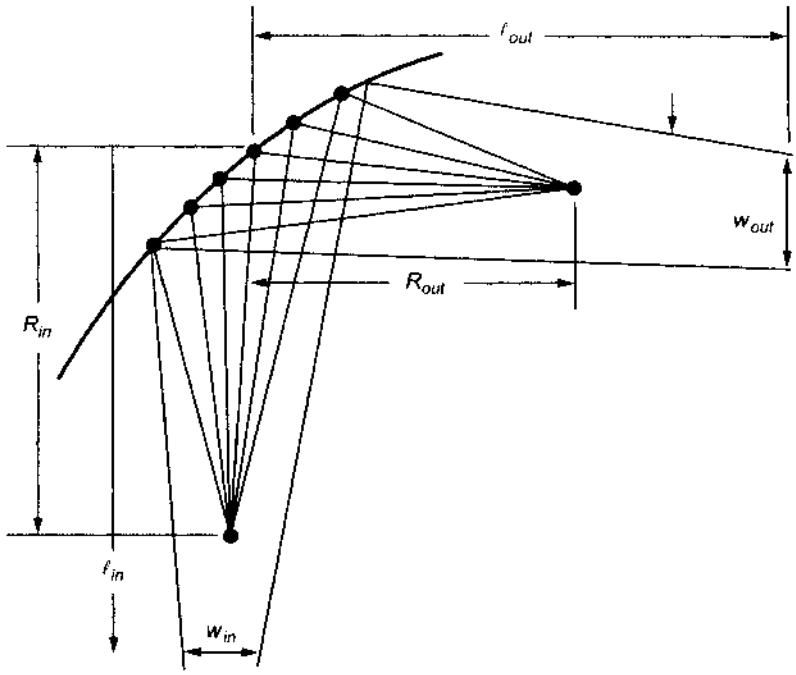

Fig. 1-13. Ray-optics approach for determining output-beam parameters.

The approach for determining the amplitudes of Gaussian-beam modes directly from reflector current will now be summarized. Note that two approximations are necessary. First, the reflector current is approximated to be the PO current—a good approximation for large reflectors with low edge illumination. Second, the Gaussian-beam modes are used as solutions to Maxwell's equations in free space—never true but a good approximation if the mode fields are required only in the paraxial region. The Gaussian-beam modes used are given in terms of Laguerre polynomials, as described by Goldsmith [27]. Each mode has a polarization, either x or y; a radial index, p; and an azimuthal index, m.

For two arbitrary fields and their associated sources, denoted by A and B, the reciprocity theorem when applied to an arbitrary volume, V, and its enclosing surface, S, may be stated as follows:

$$\oiint_S \left(\overline{E}_A \times \overline{H}_B - \overline{E}_B \times \overline{H}_A\right) ds = \tag{1.2-26}$$

$$\iiint_V \left(\overline{E}_B \bullet \overline{J}_A - \overline{\mathrm{H}}_B \bullet M_A - \overline{E}_A \bullet \overline{J}_B + \overline{\mathrm{H}}_A \bullet \overline{M}\right) dv$$

A half-space completely enclosing the reflector is chosen as V, with the surface, S, perpendicular to the direction of propagation for the output beam set. For this particular application, we choose the output Gaussian-mode set, with unknown mode amplitudes, as the A field, with the reflector current inside the volume being its source. For the B field, we choose a test field, the conjugate of the i^{th} Gaussian-beam mode now propagating toward the reflector. The source for this field is chosen to be outside the volume, V. We then have for the fields,

$$\begin{aligned} \bar{E}_A &= \sum_j a_j \bar{e}_j \\ \bar{H}_A &= \sum_j a_j \frac{\hat{z}_{out} \times \bar{e}_j}{\eta_0} \\ \bar{E}_B &= \bar{e}_i^* \\ \bar{H}_B &= -\frac{\hat{z}_{out} \times \bar{e}_i^*}{\eta_0} \end{aligned} \tag{1.2-27}$$

Using the reciprocity theorem and the orthogonality condition for the Gaussian-beam modes on the infinite surface, S, we can obtain the desired equation for the unknown coefficients:

$$a_i = -\frac{1}{2} \iint_{S_{\text{reflector}}} \bar{e}_i^* \bullet \bar{J} ds \tag{1.2-28}$$

1.2.5.3 Ray Analysis Algorithm. A bundle of rays is launched from the feed point to the first reflector. The ray density distribution in angular space is taken to be proportional to the power pattern of the input feed. The rays are then traced through the multiple reflector system. A flat plate is placed a large distance from the final mirror, perpendicular to the central ray. The rays from the final mirror are traced to the flat plate. The density distribution of the rays on the flat plate can be processed to yield the far-field pattern scattered from the last mirror.

1.2.5.4 An Example. Consider the three-curved-mirror BWG system used in the NASA/Jet Propulsion Laboratory (JPL) 34-m R&D BWG antenna (see Chapter 7 for a more detailed discussion of this antenna). The physical configuration of the BWG consists of a beam magnifier ellipse followed by an imaging pair of parabolas. The system is designed to operate from 2 to 35 GHz. Figures 1-14 and 1-15 compare the three methods at 2.3 and 32 GHz. Recall that the ray optics technique is frequency independent.

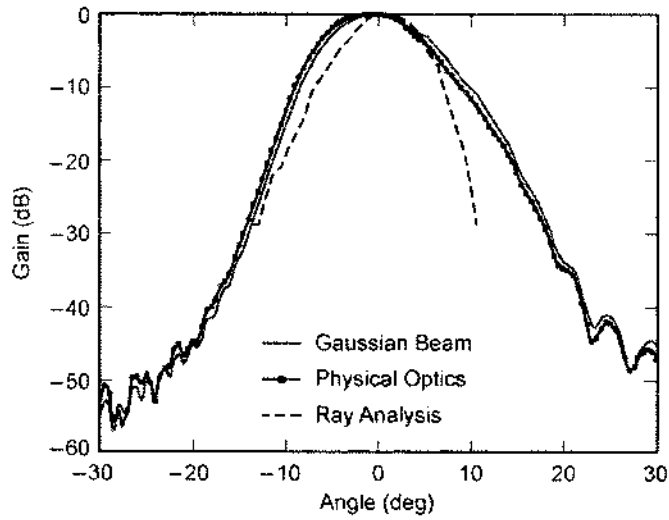

Fig. 1-14. Comparison of three methods at 2.3 GHz (S-band receive).

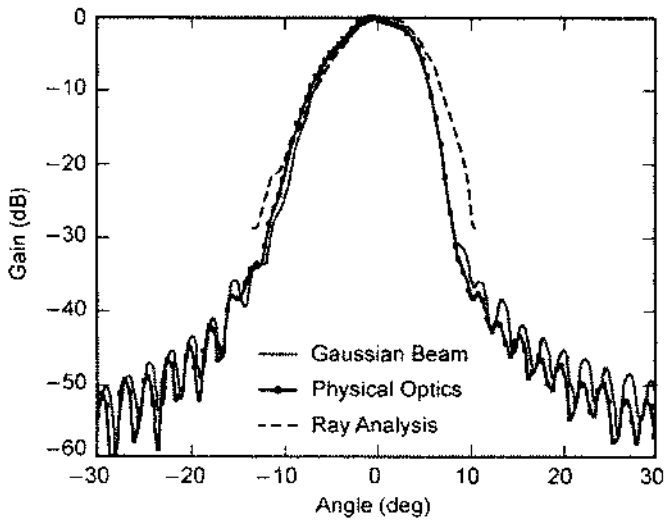

Fig. 1-15. Comparison of three methods at 32 GHz (Ka-band receive).

Of the three techniques discussed above, the PO technique is the most accurate, albeit most time consuming. For the BWG system, higher-order Gaussian modes provide a very good estimate of performance, with minimal computer time. Ray optics is generally not adequate for diffraction pattern calculations.

1.2.6 Dichroic Analysis

The ability to transmit and receive simultaneously at multiple frequency bands is an important requirement for the DSN. It is usually accomplished by using either a dual-band feed horn or separate feed horns and a frequency-selective surface (FSS), typically referred to as a dichroic plate. As dichroic plates are an important aspect of the DSN antenna design, this section presents a technique for analyzing them. For a more complete discussion of DSN use of dichroic plates, see Chapter 5 of this monograph.

The first use of a dichroic plate was as part of the reflex–dichroic feed system used on the DSN's first 64-m antenna. That plate consisted of circular holes in a half-wavelength-thick metallic plate. All subsequent dichroic plates used in the DSN were also thick plates with holes. The discussion that follows treats the most general case of the analysis of a thick dichroic plate with arbitrarily shaped holes at arbitrary angles of incidence. However, most of the plates currently in use in the DSN were designed with programs that only analyzed the simple geometries such as circular [28] or rectangular holes [29]. The technique parallels the development for the rectangular hole case except that the waveguide modes are generated using the finite-element method (FEM).

The analysis of a thick dichroic plate with arbitrarily shaped holes (Fig. 1-16) is carried out in a series of steps:

1) Construct a model of a half-space infinite array
2) Develop a complete set of basis functions with unknown coefficients for the waveguide region (waveguide modes) and for the free-space region (Floquet modes) in order to represent the electromagnetic fields

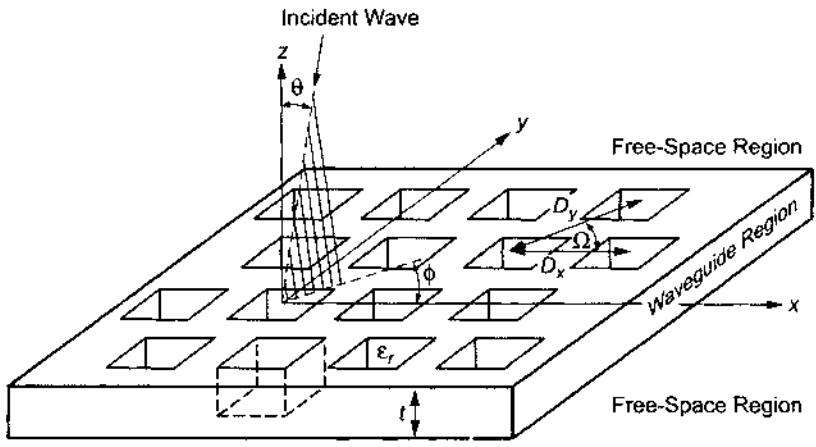

Fig. 1-16. Geometry of a thick dichroic plate with holes.

3) Apply the boundary conditions at the interface between these two regions; use the method of moments to compute the unknown mode coefficients
4) Calculate the scattering matrix of the half-space infinite array
5) Move the reference plane of the scattering matrix half-a-plate thickness in the negative z direction
6) Synthesize a dichroic plate of finite thickness by positioning two plates of half-thickness back to back
7) Obtain the total scattering matrix by cascading the scattering matrices of the two half-space infinite arrays.

The full details of the analysis are given in [30]. Since the use of Floquet modes and the method of moments to analyze dichroic plates are well documented in many references [28–32], they will not be repeated here. However, a short discussion of the use of FEM to solve the arbitrarily shaped waveguide problem will be presented. Also, an example of the most recent design of a dichroic plate will be shown.

1.2.6.1 Finite-Element Formulation of the Waveguide Problem. As is well known, the eigenmodes of a hollow, uniform waveguide may be determined by solving the 2-D scalar Helmholtz equation,

$$\left(\nabla^2 + k^2\right)\Psi = 0 \tag{1.2-29}$$

Here, Ψ represents the magnitude of an axially directed electric or magnetic Hertz vector.

Rather than attempting to solve this eigenvalue problem directly, FEM reframes it in variational terms. As is shown in [33], the solution of the Helmholtz equation with homogeneous boundary conditions is equivalent to minimizing the functional $\mathcal{F}$ defined by

$$\mathcal{F} = \iint_R \left(-\left|\text{grad}\,\varphi\right|^2 + k^2\varphi^2\right) dxdy \tag{1.2-30}$$

The region of integration is, of course, the waveguide cross section. If a trial solution, $\varphi(x,y)$, is represented geometrically as a function spanning the region, R, over the x,y plane, the correct function, $\Psi(x,y)$, is that which yields the smallest possible value of $\mathcal{F}$.

Using a surface function, $\varphi(x,y)$, made up of finite surface elements of a simple kind, FEM approximates the correct solution. For simplicity, all the elementary regions are taken to be triangles. Corresponding to each elementary

region, the surface element will be defined by requiring that $\varphi(x,y)$ be a linear function of its values at the vertices; thus, φ is defined by

$$\varphi(x,y) = \sum_{i=1}^{N} \alpha_i(x,y)\,\varphi_i \tag{1.2-31}$$

$\mathcal{F}$ is now an ordinary function of the parameters that define φ, in this case the vertex values φ_i:

$$\mathcal{F}(\varphi) = F(\varphi_1, \varphi_2, \cdots, \varphi_N) \tag{1.2-32}$$

The solution is found by minimizing F with respect to all the parameters. That is, it will be required that

$$\frac{\partial \mathcal{F}}{\partial \varphi_m} = 0 \tag{1.2-33}$$

for all m. If the region, R, contains altogether N vertices, this minimization requirement changes Eq. (1.2-30) into a matrix eigenvalue problem of order N.

In view of Eq. (1.2-32), the minimization requirement, Eq. (1.2-33), is equivalent to

$$\iint_R \frac{\partial}{\partial \varphi_m} |\text{grad}\,\varphi|^2 \, dxdy = k^2 \iint_R \frac{\partial}{\partial \varphi_m} \varphi^2 dxdy \tag{1.2-34}$$

As is shown in [30], if we define the purely geometrical quantities

$$S_{mk} = \iint_R \left(\frac{\partial \alpha_m}{\partial x}\frac{\partial \alpha_k}{\partial x} + \frac{\partial \alpha_m}{\partial y}\frac{\partial \alpha_k}{\partial y} \right) dxdy \tag{1.2-35}$$

and

$$T_{mk} = \iint_R \alpha_m \alpha_k \, dxdy \tag{1.2-36}$$

which expresses the nature of the region R and the manner of its subdivision into elementary regions, then, in terms of these integral quantities, Eq. (1.2-34) reads

$$S\Phi = k^2 T\Phi \tag{1.2-37}$$

where Φ is the column matrix of vertex values φ_i, and S and T are square matrices of order N, whose elements are S_{mk} and T_{mk}, as defined above. Minimization of $\mathcal{F}$ is thus equivalent to the eigenvalue problem, Eq. (1.2-37), and

solution of the latter will provide approximate eigenvalues and eigenfunctions for the boundary-value problem. Note that S and T are always symmetric, and the eigenvalues, therefore, always real.

1.2.6.2 Low-Cost Dichroic Design. As stated earlier, most of the plates currently in use were designed with programs that analyzed only the simple geometries, such as circular or rectangular holes. Since it is too expensive to experimentally determine FSS parameters, only designs that could be accurately analyzed were chosen, and since it is expensive to empirically design the dichroic plates, the earliest FSS designs used rectangular holes. To achieve the sharp corners of the rectangular holes, it was necessary to use an electrical discharge machining (EDM) manufacturing technique. This manufacturing technique is expensive, and an important use of the arbitrarily shaped analysis is to enable designs that use rounded corners, which can be manufactured less expensively. An example of a manufacturing test sample for an X-/Ka-band dichroic plate is shown in Fig. 1-17. The plate is designed to pass the Ka-band receive frequencies (31.7–32.2 GHz) and reflect both the X-band transmit (7.145–7.190 GHz) and receive (8.4–8.5 GHz), and it is a direct replacement for the X-/Ka-band plate [34] currently in use in the BWG antennas. It was manufactured using an end-milling technique and cost one-fourth the price of an equivalent-sized EDM-manufactured plate. An example of FEM gridding is shown in Fig. 1-18.

Since the analysis of arbitrarily shaped holes is quite new, only designs using rectangular holes are currently installed in DSN BWG antennas. The calculated and measured reflection coefficient of the X-/Ka-band dichroic plate used in the 34-m BWG antennas is shown in Fig. 1-19 [34].

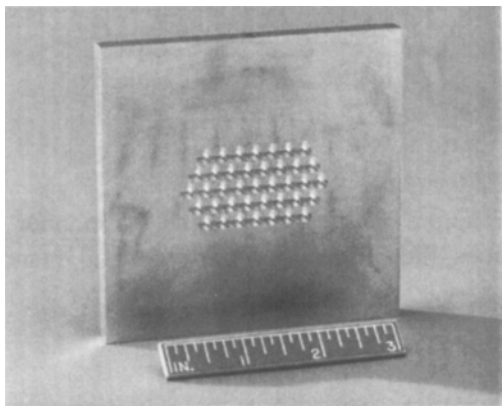

Fig. 1-17. Manufacture test sample for the X-/Ka-band dichroic plate with rounded corners.

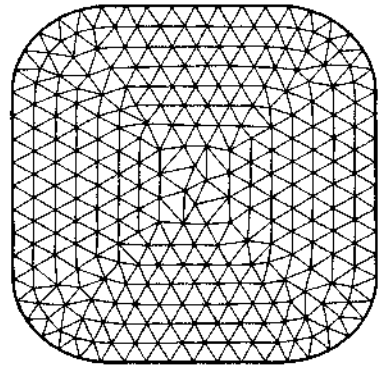

Fig. 1-18. Finite-element gridding of the rectangular hole with rounded corners.

1.2.7 Antenna Noise-Temperature Determination

The system-noise temperature of a receiving system is the sum of the receiver-noise temperature and the antenna temperature. The individual contributions to the antenna temperature include cosmic radio noise, atmospheric absorption, thermal radiation from the ground, and transmission line loss.

The noise temperature of an antenna is defined [2] as

$$T_a = \frac{P_A}{kB} \tag{1.2-38}$$

where P_A is the noise power delivered by the antenna over a bandwidth, B, into a matched termination, and k is Boltzman's constant, equal to 1.380×10^{-23} J/K.

Also, the effective antenna noise temperature can be expressed as the radiation pattern-weighted environmental black body temperature $T(\Omega)$ averaged over all directions; thus,

$$T_a = \frac{1}{4\pi} \int_{4\pi} T(\Omega)G(\Omega)d\Omega = \frac{\int_{4\pi} T(\Omega)P(\Omega)d\Omega}{\int_{4\pi} P(\Omega)d\Omega} \tag{1.2-39}$$

where $G(\Omega)$ is the antenna gain in the direction Ω, and $P(\Omega)$ is the normalized antenna pattern gain in direction Ω, or

$$P(\Omega) = \frac{G(\Omega)}{G_m} \tag{1.2-40}$$

with G_m the antenna maximum gain.

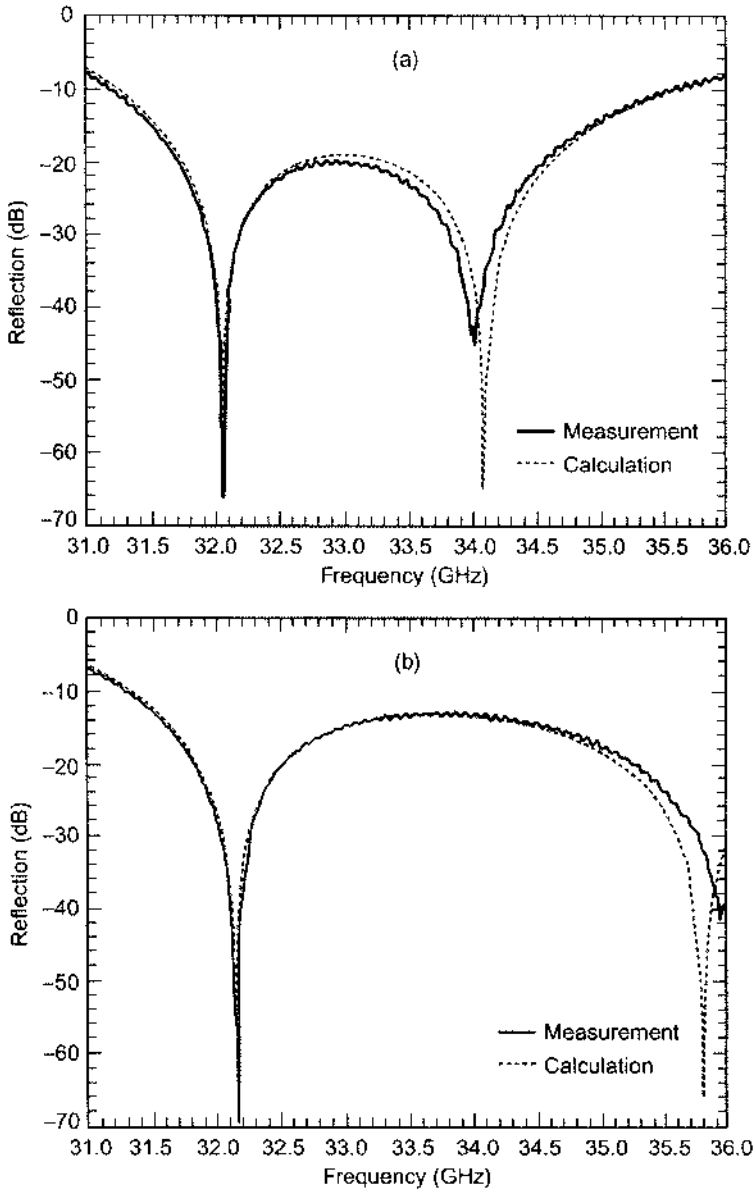

Fig. 1-19. Calculated and measured reflection coefficient versus frequency for the X-/Ka-band/KABLE-band dichroic plate: (a) TE polarization and (b) TM polarization.

Evaluation of Eq. (1.2-39) may range from rough approximations or rules of thumb to a very painstaking evaluation by numerical integration of the functions involved.

1.2.7.1 Noise Temperature in BWG Systems. At the start of the BWG antenna project (discussed in Chapter 7), noise-temperature contributions due to BWG mirror spillover were not clearly understood. It was at first assumed that spillover power was eventually absorbed by cold sky or by a cold front-end receiver. However, this assumption was incorrect, and an empirical relationship between the calculated spillover energy and noise temperature was developed [35]. When attempting to use the empirical data from one BWG design to predict performance of another design also proved to be erroneous, it became apparent that an accurate analytic procedure that included the effects of the BWG shroud was required [36–39].

The major contributors to noise temperature in a BWG are the spillover past the mirrors and the conductivity loss in both the BWG shroud walls and reflecting mirrors.

The analytical method extends the approach of [36], which computes the waveguide modes that are propagating in the oversized waveguides. Reference [36] describes a PO integration procedure of the currents of the BWG mirrors, using a Green's function appropriate to the circular-waveguide geometry. Once all the modes in the waveguide are known, it is a simple matter to use standard approximations to determine the attenuation constant and, thus, the conductivity loss if the conductivity of the wall material is known. Also, all energy that propagates toward, but spills past, a BWG mirror is assumed to be lost in the walls of the BWG as well. The noise temperature is computed assuming both loss components are exposed to ambient temperature. The conductivity loss in the reflecting mirrors is a straightforward calculation, and the corresponding noise temperature is linearly added to the other noise contributors.

The BWG tube analysis is conceptually similar to the PO analysis used in reflector-antenna analysis. Currents induced in the BWG mirror are obtained using a standard PO approximation of $J = 2\hat{n} \times H_{inc}$, where $\hat{n}$ is the surface normal and H_{inc} is the incident field. However, the BWG analysis differs in the methods by which the incident field on a mirror and the scattered field radiated from the mirror are calculated.

One approach to calculating the scattered field is to use a dyadic Green's formulation [36], where the field scattered from a BWG mirror is computed using the Green's function appropriate to the cylindrical waveguide geometry.

While it is conceptually convenient to use Green's functions to discuss the comparison with PO, the actual computation using this approach is rather cumbersome. Instead, a simpler method is used to calculate waveguide fields, based upon the reciprocity theorem. The basic problem is to find the fields radiated by

an arbitrary current (the PO currents on the reflector) in a cylindrical waveguide. The problem is easily solved by expanding the radiated field in terms of a suitable set of normal modes, with amplitude coefficients determined by an application of the Lorentz reciprocity theorem [38].

An arbitrary field in a waveguide can be represented as an infinite sum of the normal modes for the guide. Let the normal modes be represented by (see Fig. 1-20)

$$\begin{aligned} \overline{E}_n^{(\pm)} &= \left(\overline{e}_n \pm \overline{e}_{zn}\right) e^{\mp \Gamma_n z} \\ \overline{H}_n^{(\pm)} &= \left(\pm \overline{h}_n + \overline{h}_{zn}\right) e^{\mp \Gamma_n z} \end{aligned} \tag{1.2-41}$$

where $\overline{E}_n^{(+)}$ represents a mode traveling in the $+z$ direction, and $\overline{E}_n^{(-)}$ is a mode traveling in the $-z$ direction. For a basic normal mode description, see [40].

Let the field radiated in the $+z$ direction by the current be represented by

$$\begin{aligned} \overline{E}^{(+)} &= \sum_n a_n \overline{E}_n^{(+)} \\ \overline{H}^{(+)} &= \sum_n \frac{a_n}{Z_n} \overline{H}_n^{(+)} \end{aligned} \tag{1.2-42}$$

and the field radiated in the $-z$ direction by

$$\begin{aligned} \overline{E}^{(-)} &= \sum_n b_n \overline{E}_n^{(-)} \\ \overline{H}^{(-)} &= \sum_n \frac{b_n}{Z_n} \overline{H}_n^{(-)} \end{aligned} \tag{1.2-43}$$

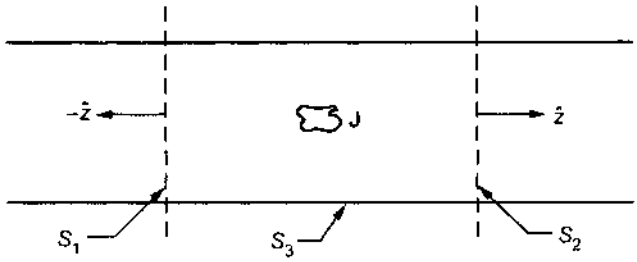

Fig. 1-20. Geometry for computing waveguide modes.

An application of the Lorentz reciprocity theorem [38] can show that

$$\begin{aligned} a_n &= -\frac{1}{2} Z_n \int_v \left[\bar{E}_n^{(-)} \bullet \bar{J}\right] dV \\ b_n &= -\frac{1}{2} Z_n \int_v \left[\bar{E}_n^{(+)} \bullet \bar{J}\right] dV \end{aligned} \tag{1.2-44}$$

where $\bar{J}$ is the volume current in the waveguide.

Since we have only surface currents, the integral for the PO currents is over the surface of the reflector. If we let

$$c_n = -\frac{1}{2} \int_s J_s \bullet \bar{E}_n^{(-)} ds \tag{1.2-45}$$

where J_s is the PO currents on the mirror, then

$$\begin{aligned} \bar{H}^+ &= \sum_n c_n \bar{H}_n^{(-)} \\ \bar{E}^+ &= \sum_n Z_n c_n \bar{E}_n^{(-)} \end{aligned} \tag{1.2-46}$$

and the total power contained in the fields is

$$P = \sum_n Z_n |c_n|^2 \tag{1.2-47}$$

If the spillover past the mirror is small (that is, >25-dB edge taper), the PO currents induced on the first mirror are computed in the standard way, by utilizing the free-space near-field radiating H-field of the horn and $J_s = 2\hat{n} \times H_{inc}$. Or they may be computed by utilizing a technique similar to the one just described to compute the propagating modes from the horn, radiating in the oversized waveguide and using the appropriate H-field derived from these modes as the incident field. On subsequent mirrors, PO currents are computed from the H-field derived from the propagating waveguide modes. The technique is summarized in Fig. 1-21, where it should be noted that

$$H = \int_s \bar{J}_1 \bullet \bar{\bar{G}}_{wg} ds = \sum_n c_n \bar{H}_n^{(-)} \tag{1.2-48}$$

Power loss in the conductor is obtained using the standard technique to compute the power dissipated in the conductor per unit length [39] as

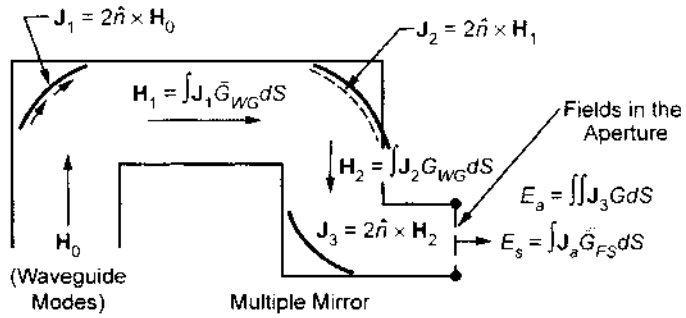

Fig. 1-21. Computation of fields in the BWG system.

$$P_d(z) = R \int_0^{2\pi} \left|\overline{H}_t\right|^2 a d\phi \tag{1.2-49}$$

where

$$R = \sqrt{\frac{\omega\mu}{2\sigma}} \tag{1.2-50}$$

and σ is the wall conductivity, a the radius, and $\left|\overline{H}_t\right|^2$ the tangential **H** field. It should be noted that P_d is a function of z since $\left|\overline{H}_t\right|^2$ is a function of z (because it is composed of more than one waveguide mode).

Power loss is computed from

$$P = P_o e^{-2\alpha d} \tag{1.2-51}$$

where d is the distance from z_1 to z_2, and the attenuation constant is computed as

$$\alpha d = \frac{\int_{z_1}^{z_2} P_d(z) dz}{2P_f} \tag{1.2-52}$$

where P_f is the power flow in the waveguide.

To compute noise temperature, it is convenient to separate the total RF power originating from the horn aperture (viewed in transmission, for convenience) and propagating into two parts

$$P_{BWG} = P_m + P_{spill} \tag{1.2-53}$$

where P_{spill} is the portion that spills past the mirrors (since the mirrors do not fill the waveguide). The value of P_{spill} can be computed for each mirror by integrating the total power radiated from the induced mirror currents and comparing it to the incident power. Note that the computation uses the induced currents derived from the waveguide modes. It is then assumed that this spillover power is exposed to ambient temperature since it would be lost in the tube due to multiple bounces in a lossy material.

Noise temperature, then, is composed of two parts: the noise due to the spillover power added to the noise from the attenuation of P_m due to the conductivity loss.

Total noise temperature also includes the contribution from the conductivity loss in the mirrors. Noise temperature due to conductivity loss is given as

$$T_m = \left(1 - \frac{2R^2 - 2R\eta + \eta^2}{2R^2 + 2R\eta + \eta^2}\right) T_{amb} \tag{1.2-54}$$

where R is computed from the mirror conductivity, η is the free-space impedance and T_{amb} is the ambient temperature.

An example of computing noise temperature is given in Table 1-2 for the Deep Space Station (DSS-13) R&D antenna (whose design and performance is fully described in Chapter 7). The table shows the calculated [37] and measured [41] noise temperature at 8.4 GHz (X-band receive) for two different feed horns in the DSS-13 pedestal room. The spillover energy for both feed horns is shown in Table 1-3. Assuming a 290-K ambient temperature, the noise-temperature contribution is shown in Table 1-2. The shroud is steel with conductivity of 0.003×10^7 mhos/m, and the noise-temperature contribution is also shown in Table 1-2. The mirrors for both feed horns are machined aluminum with conductivity of 3.8×10^{-7} mhos/m. The loss for one mirror is 0.001 dB, with a corresponding noise temperature of 0.094 K. The noise-temperature contribution for all six mirrors is 0.564 K.

Observe that the major contributor to noise temperature in a BWG system is the spillover energy past the mirrors. On the other hand, contribution from

Table 1-2. DSS-13 noise temperature at 8.4 GHz (X-band receive mode): measured versus calculated.

Feed-Horn Gain	Noise Temperature (K)				
	Spillover Energy	Shroud Conductivity	Mirror Conductivity	Total Calculated	Total Measured
22.5-dB	7.95	0.24	0.564	8.75	8.9
24.2-dB	0.93	0.05	0.564	1.54	2.0

Table 1-3. Spillover energy in the DSS-13 BWG system (X-band transmit mode).

Mirror	Spillover (percent)			
	22.5-dB Feed Horn		24.2-dB Feed Horn	
	Each Mirror	Total	Each Mirror	Total
M6	0.36	0.36	0.00	0.00
M5	1.02	1.38	0.12	0.12
M4	0.25	1.63	0.00	0.12
M3	1.04	2.67	0.20	0.32
M2	0.04	2.71	0.00	0.32
M1	0.03	2.74	0.00	0.32

the conductivity loss in both the mirrors and shroud is small. The analytical technique that includes the effects of the shroud has been shown to be a reasonably accurate method to predict noise temperature.

1.3 Measurement Techniques

A number of sophisticated measurement techniques are required to properly characterize the performance of a large reflector antenna. First, there is a need to accurately measure the main reflector surface. This measurement is determined either by theodolite or microwave holography. Second, measuring gain or efficiency is required, and third, noise temperature.

1.3.1 Theodolite Measurements

Theodolite measurements are typically used in the initial alignment of the antenna after installation of the reflector panels. The method of determining the reflector surface is based on angular measurements made with a theodolite [42,43]. The theodolite is placed at the main reflector vertex and is used to measure the angles to targets installed at the individual reflector panel corners. After the panels are installed on the antenna, the surface panels are drilled using the holes in a metal strap gauge as a template for placing targets.

Errors in theodolite measurements are due to uncertainty in the angular measurement of the target position and radial distance to the target. At a radius of 13 m, which is the surface area median radius for a 34-m antenna, a 0.001-deg error in the angle to the target corresponds to a 0.2-mm error normal to the surface; a 1.0-mm error in the radial distance corresponds to a 0.26-mm error normal to the surface.

A typical error budget [43] for the surface error budget of a 34-m antenna is 0.3-mm root-sum-square (rss). By far, the greatest source of error is in the radial distance measurement provided by using a drill tape. If, instead, a laser range finder is used to measure radial distance, the error could improve from 0.3-mm rms to 0.2-mm rms. In any case, microwave holography has been used to characterize and reset the main reflector surface after initial operation, using the theodolite-set panels.

During 2000 and 2001, a Leica TDM-5000 "total station" theodolite was used to measure all three of the DSN 70-m antennas [44]. The instrument measures vertical and horizontal angles and distances, downloads them to a desktop computer, which converts the coordinates from the spherical to a Cartesian system and can be used to command the instrument to motor to a desired look angle.

Theodolites are used to measure DSN antennas in the following manner: The theodolite is bolted securely to the bracket close to the center of the main reflector. The theodolite's gravity compensator is turned off so that it will rotate with the reflector.

Targets are placed in 12 concentric rings, wherever cables, supports, or other equipment in the feed support structure do not block the view. The targets are made up of 20-mm, square pieces of tape, 0.33-mm thick, attached to the front face of black plastic mounts such that the visible target crosshair is 11.15 mm above and normal to the local reflector surface. The estimated target height variation is on the order of ± 0.38 mm. See [44] for photographs of the targets and visible target placements.

The total station theodolite described above measures distance and angles from the instrument to the target on the reflector surface. The measurement geometry is shown in Fig. 1-22. The range and angle data is used to compute the error normal to the reflector surface for surface adjustment or to determine the half-path-length error for antenna efficiency calculations.

The major error contributors are the angle reading error, distance measurement error, and targeting error. However, by viewing a target as closely as possible to tangent to the surface, the effect of distance measurement error inherent

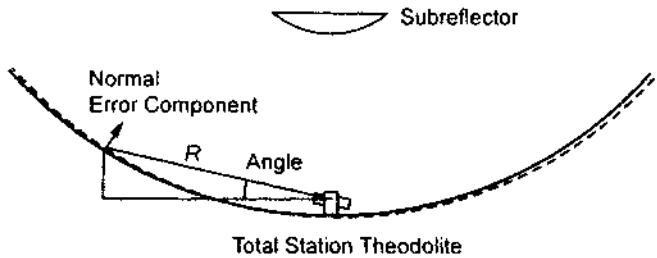

Fig. 1-22. Reflector measurement geometry.

in the theodolite is minimized. In the worst case, the farthest target is 36.44 m from the vertex of the main reflector. Using this distance with the estimated operator angle accuracy of ± 3 arcsec gives a peak surface-normal measurement error of ± 0.5 mm.

For a parabolic main reflector with a theodolite at the vertex, the slope of the theodolite line-of-sight to any target is half of the parabola surface slope at the target. For the 70-m shaped main reflector with a nominal focal length of 27.05 m, the edge slope at 35-m radius is 33 deg, so the reflector surface is tilted by as much as 16.5 deg to the theodolite line-of-sight. Based on a distance measurement error of 1.3 mm, this component of the measurement error is 1.3 tan (16.5 deg) = ± 0.38 mm.

Figure 1-23 shows the estimated 1-sigma measurement error normal to the surface as a function of distance from the instrument to the target. The angle, range, and targeting error components are shown with the rss total and the area weighted 1-sigma rms half-path-length error of 0.17 mm.

The reflector coordinate system is based on a reference file created from the nominal target locations. First, the nominal target coordinates are calculated based on the measured reflector surface arc length, circumferential spacing, and reflector radial surface shape. Then, they are combined into a reference file. The theodolite system motors to the nominal location of each target, the target is placed precisely in the theodolite crosshairs, then measured and recorded. When all of the targets are measured the first time at zenith, the data is best-fit to the theoretical coordinates in the reference file to transform the coordinates from a theodolite-centered coordinate system to the reflector system. No reference points, which might indicate the true reflector optics, are used in any of the measurements. The recorded target locations thus

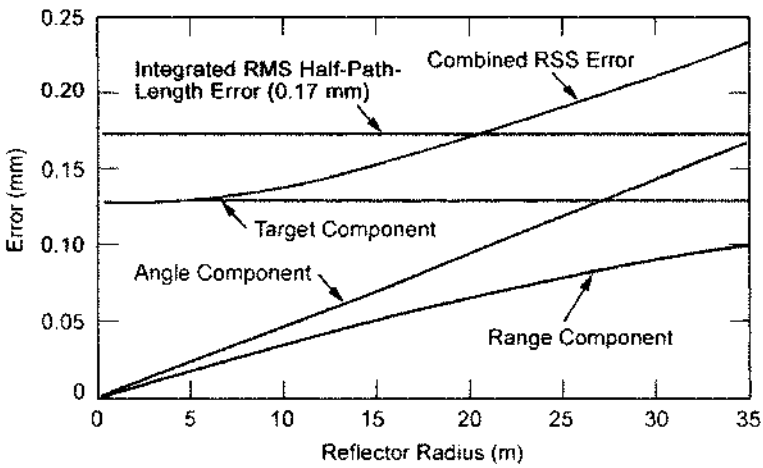

Fig. 1-23. Measurement error (1 sigma).

transformed become the new reference target file used in all subsequent measurements.

The measured data is fit to the theoretical surface of the shaped main reflector. Residual surface errors at each point are determined and rms accuracy of the surface computed. Results are presented as half-path-length errors (HPLEs) in millimeters. The HPLE is the usual presentation of surface errors, which relates surface rms to gain loss [45].

Table 1-4 shows the calculation of the rms errors after best-fitting for all three 70-m antennas. The best-fitting applied performs a least-squares fit using six degrees of freedom: translation in x, y and z; rotation about x and y; and focal point adjustment, since there is a motorized subreflector. The first data row is for all measured points. The second row removes the inner panel, which is blocked by the subreflector, and the outer panel, which is not included in the alignment derived from the holographic measurement.

With minor adjustments to the theodolite and a comfortable working platform for the operator, primary surface and subreflector position measurements as described above can be performed at any elevation angle for a tracking antenna. For antenna structures that behave in a linear elastic fashion, measurements at three separate elevation angles provide sufficient information to determine the relative positions of all targets at any other angle. (A common example of nonlinear structural deformation is the bending of bolted flanges.) The process requires the intermediate calculation of the face-up (zenith-pointing) and face-side (horizon-pointing) gravity deformations of the reflector, and their subsequent vector superposition. The best results will be achieved if the elevation angles at which measurements are made are well separated, such as 0, 45, and 90 deg. For the 70-m antennas, the analysis was based on measurements made at 13, 47, and 89 deg.

The gravity deformation of a linear elastic structure at any elevation angle can be derived by vector superposition for the face-up and face-side gravity vectors as

$$\delta = \delta_u \sin\theta + \delta_s \cos\theta \qquad (1.3\text{-}1)$$

where

δ_s = face-side gravity deformation

δ_u = face-up gravity deformation.

The face-up and face-side deformations described here are of the type derived from a computer structural analysis in which gravity is "turned on" from a particular direction. As such, the deformations cannot be directly measured in the real world.

Table 1-4. Measured rms errors for all antennas.

RMS	13-deg Elevation Angle			30-deg Elevation Angle			47-deg Elevation Angle			68-deg Elevation Angle			89-deg Elevation Angle		
	DSS			DSS			DSS			DSS			DSS		
	14	43	63	14	43	63	14	43	63	14	43	63	14	43	63
All targets (mm)	1.32	1.30	1.42	N/A[a]	1.24	1.50	1.19	1.32	1.24	1.52	1.45	1.42	1.62	1.62	1.70
Inner and outer targets removed (mm)	1.07	0.97	1.22	N/A	0.79	1.14	0.84	0.84	0.91	1.07	1.04	1.09	1.27	1.24	1.50

[a]Not available.

For a linear elastic structure that rotates from angle θ_1 to θ_2, the relative deformation, or motion, will be $\delta_2 - \delta_1$, as shown above. For three measurements, two independent linear equations can be written for $\delta_2 - \delta_1$ and $\delta_3 - \delta_1$

$$\begin{bmatrix} \delta_u \\ \delta_s \end{bmatrix} = \begin{bmatrix} \sin\theta_2 - \sin\theta_1 & \cos\theta_2 - \cos\theta_1 \\ \sin\theta_3 - \sin\theta_1 & \cos\theta_3 - \cos\theta_1 \end{bmatrix}^{-1} \begin{bmatrix} \delta_2 - \delta_1 \\ \delta_3 - \delta_1 \end{bmatrix} \tag{1.3-2}$$

Now that δ_u and δ_s are known, for any angle θ, the predicted alignment error at a target is the gravity deformation traveling from a measured reference angle (θ_2) to angle θ superposed onto the actual measured alignment error at the reference angle (δ_θ). This can be expressed as

$$\begin{aligned} \delta(\theta) = \delta_\theta &+ \delta_u(\sin\theta_2 - \sin\theta) \\ &+ \delta_s(\cos\theta_2 - \cos\theta) \end{aligned} \tag{1.3-3}$$

It is possible to use measurements at more than three angles and develop an overdetermined set of equations for δ_u and δ_s that can be solved in a least-squares sense. This would help average errors in the individual datasets.

The gravity analysis of DSS-43 (the 70-m antenna near Canberra, Australia) was performed using measurements from 13, 47, and 89 deg of elevation. The predicted HPLE at each of the measured points was calculated at 5-deg elevation intervals from 0 to 90 deg, plus 13, 30, 47, 68, and 89 deg, using the actual measured data. By definition, the predictions at 13, 47, and 89 deg perfectly matched the input data.

The above process was repeated, recording the predicted gravity deformations with respect to the nominal rigging angle of 47 deg.

The rms data is summarized in Fig. 1-24. The curves show that the measured data at 30 and 68 deg closely matches the predicted values.

Using the all-angle main reflector surface shape data in a PO calculation, with the 70-m feed and subreflector configuration, an efficiency value was determined for all three antennas. The value is shown in Fig. 1-25. This predicted efficiency value is compared to the measured efficiency at DSS-14 shown in Fig. 1-26. It is interesting to note that all three 70-m antennas have similar distortions due to gravity.

1.3.2 Microwave Holography

Microwave holography [46–48] has proven to be a valuable technique for characterizing the mechanical and RF performance of large reflector antennas. This technique utilizes the Fourier transform relation between the far-field radiation pattern of an antenna and the aperture-field distribution. Resulting aperture phase and amplitude data can be used to characterize various performance

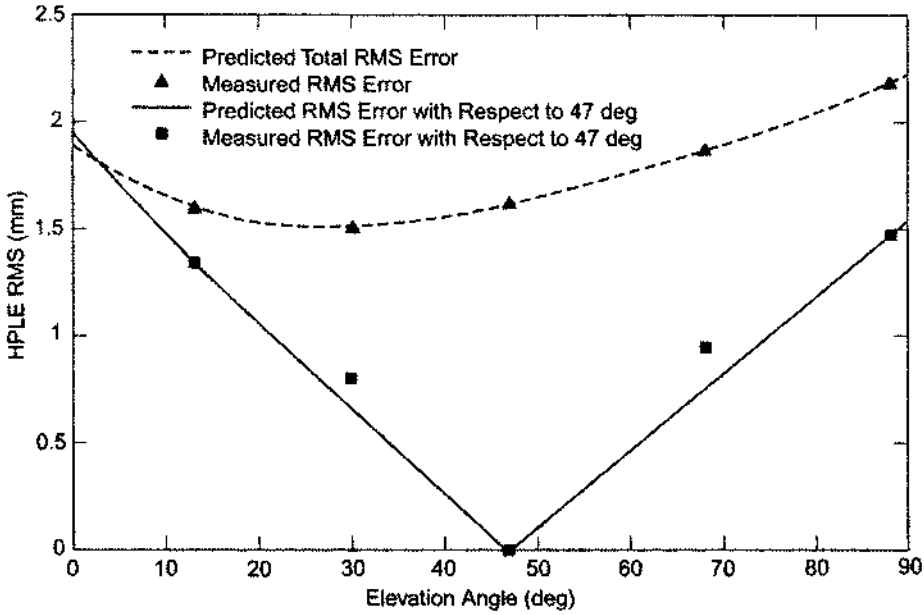

Fig. 1-24. Summary of predicted versus measured surface rms and gravity deformation for DSS-43.

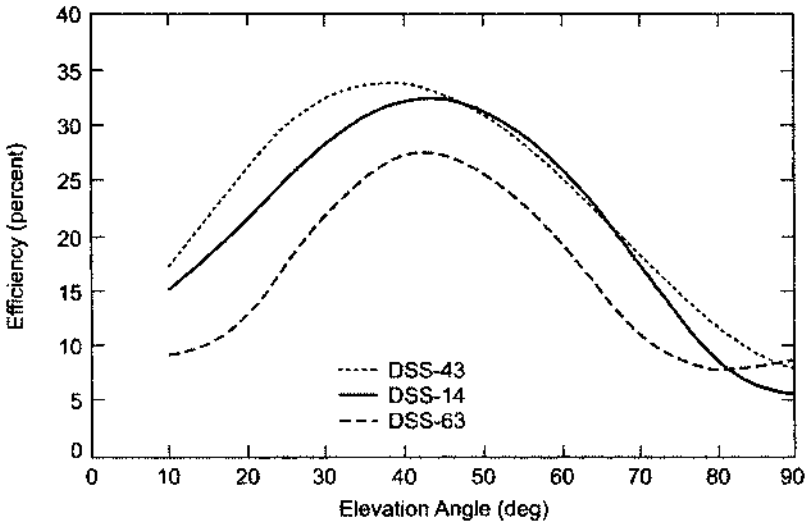

Fig. 1-25. Computed efficiencies derived from main reflector surface measurements.

parameters, including panel alignment, panel shaping, subreflector position, antenna aperture illumination, and gravity deformation effects.

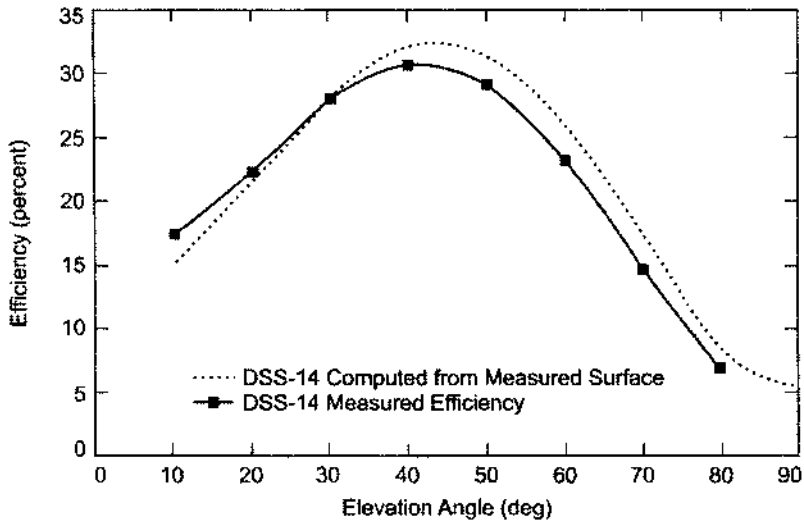

Fig. 1-26. Computed and measured 70-m antenna efficiencies for DSS-14.

The raw data (the observable) for this technique is the complex far-field pattern of the antenna under test. For large reflector antennas, geostationary satellites are commonly used as far-field signal sources. Figure 1-27 presents a typical narrowbandwidth receiver system architecture based on a Hewlett-Packard P8510B analyzer and an external phase-locked loop (PLL) (with a variable PLL bandwidth of 1 to 20 Hz) used for receiving the narrowband beacon signal from the satellite. The reference antenna is needed as a phase reference for the measurement as well as to keep the receiver in phase lock with the carrier [49,50].

The mathematical details for microwave holography are given in [47], among others, and are repeated here for completeness.

The mathematical relationship between an antenna far-field radiation pattern (T) and the antenna surface-induced current distribution (J) is given by the exact radiation integral [51]

$$\tilde{T}(u,v) = \iint_S \tilde{J}(x',y')\, e^{ikz'}\left[e^{-jkz'(1-\cos\theta)}\right] e^{j(ux'+vy')}\, dx'dy' \qquad (1.3\text{-}4)$$

where

$z'(x', y')$ = surface, S
(u,v) = directional cosine space
θ = observation angle.

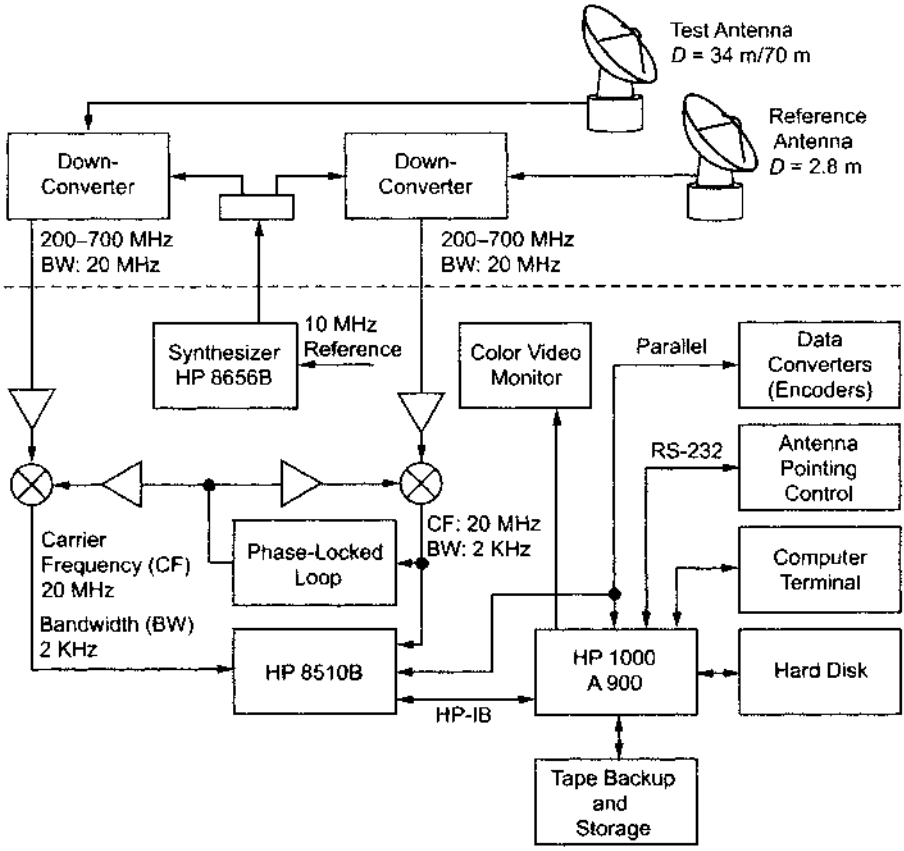

Fig. 1-27. Holography measurement block diagram.

For small observation angles of the far-field pattern, this expression becomes a Fourier transform relationship

$$\vec{T}(u,v) = \iint_{s} \vec{J}(x',y')\, e^{jkz'}\, e^{jk(ux'+vy')}\, dx'dy' \qquad (1.3\text{-}5)$$

To derive the residual surface error, GO ray tracing is used to relate the small normal error, ε, directly to an aperture phase error in a main reflector paraboloid geometry (Fig. 1-28). In this small error approximation, it is assumed that the aperture phase error is entirely due to the projected surface errors. In addition, the 3-D structure of the surface error is not recovered; rather, an axial component equal to the average error over the resolution cell size is recovered. The normal error can then be computed using the paraboloid geometry.

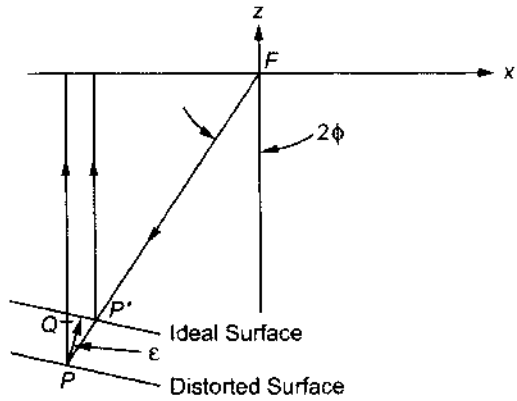

Fig. 1-28. Surface-distortion geometry.

The path length is related to the phase as

$$\text{Phase} = \frac{4\pi\varepsilon}{\lambda}\cos\phi \tag{1.3-6}$$

with

$$\cos\phi = \frac{1}{\sqrt{1+\dfrac{x^2+y^2}{4F^2}}} \tag{1.3-7}$$

for a parabola.

Allowing for the removal of a constant phase term and substituting Eq. (1.3-6) into Eq. (1.3-5) yields:

$$T(u,v) = e^{-j2kF}\iint_S \left[\left|\tilde{J}(x',y')\right| e^{j4\pi\varepsilon/\lambda\cos\phi} e^{jkz'}\right] e^{jk(ux'+vy')}dx'dy' \tag{1.3-8}$$

where $[\ldots] \equiv J_e$ (equivalent current distribution).

For the processing of sampled data, the associated discrete Fourier transform (DFT) is used:

$$T(p\Delta u, q\Delta v) = sxsy \sum_{n=-N1/2}^{N1/2-1} \sum_{m=-N2/2}^{N2/2-1} J(nsx, msy)\, e^{j2\pi\left(\frac{np}{N1}+\frac{mq}{N2}\right)} \tag{1.3-9}$$

where

$N1, N2$ = measured data array size

sx, sy = sampling intervals in the aperture coordinates

n, m, p, q = integers indexing the discrete samples

$\Delta u, \Delta v$ = sampling intervals in u, v far-field space.

Since the magnitude of the far-field pattern is essentially bounded, the fast Fourier transform (FFT) is generally used for computation and is symbolized here by F. Solving for the residual normal surface error and substituting Eq. (1.3-7) yields

$$\varepsilon(x, y) = \frac{\lambda}{4\pi} \sqrt{1 + \frac{x^2 + y^2}{4F^2}} \text{ Phase } \left\{ e^{j2kF} \mathcal{F}^{-1}[T(u,v)] \right\} \qquad (1.3\text{-}10)$$

Accuracy across the holographic map varies with aperture amplitude illumination. Accuracy is better at the center of the dish and gradually worsens toward the edge, where illumination falls off rapidly. For a uniformly illuminated antenna design, accuracy remains relatively constant, becoming quickly worse just at the edge, also where the illumination falls off rapidly. Typically, accuracies of 0.05 mm to 0.10 mm were achieved with a corresponding signal-to-noise ratio (SNR) of 73 dB to 60 dB.

The resulting aperture phase function needs to be corrected for modulo-2π phase errors, which occur due to the small measurement wavelength and a large phase error that is partially caused by pointing and subreflector position errors. Next, it is necessary to remove phase errors due to pointing and subreflector position errors, and this is done via the global best-fit paraboloid. Here, the entire dataset is weighted-least-squares-fitted to the paraboloid, permitting six degrees of freedom in the model, three vertex translations, two rotations, and a focal length change. The antenna surface axial rms error is then computed with respect to the position of the fitting paraboloid.

The resultant aperture function at the end of this process is defined here as the effective map, since it includes all phase effects contributing to antenna performance. These frequency-dependent effects include subreflector scattered (frequency-dependent) feed phase function and diffraction effects due to the struts. Removal of the feed phase function and subreflector support structure diffraction effects results in a frequency-independent map, which is defined here as the mechanical map. In general, the panel-setting information is derived from the mechanical map, since the antenna needs to be operated over a range of frequencies. Panel-setting information is derived by sorting all the data points within each panel and performing a rigid-body least-squares fit. The algorithm allows for one translation and two rotations.

1.3.3 Aperture Gain and Efficiency Measurements

Determination of aperture efficiency follows a JPL-developed methodology [52,53]. For a radio source of known flux density, the increase in system-noise temperature as determined by the boresight measurements is a measurement of antenna efficiency.

Peak radio source noise temperatures are measured via a boresight algorithm [54]. These measured quantities are then normalized by T_{100}/C_r, where T_{100} is the 100 percent antenna efficiency temperature, and C_r is the source size-correction factor [52,55]. Values of the temperature $T_a = T_{100}/C_r$ for radio sources used to calibrate DSN antennas are given in [56]. The effects of atmospheric attenuation must also be considered; for this reason, the final measured values are then corrected for yield vacuum conditions.

The typical method used to measure system-noise temperature in DSN antennas is the seven-point boresight technique. This method moves the antenna sequentially in both the cross-elevation (XEL) and elevation (EL) direction, both on- and off-source. In each direction, the antenna is positioned off-source 10 half-power (one-sided) beamwidths; one half-power beamwidth at the 3-dB point; approximately 0.576 half-power beamwidths at the 1-dB point; on-source; and then similar offsets on the other side. For example, at X-band with the 34-m antenna, the full 3-dB beamwidth is 65 mdeg. The offsets used were 325, 32.5, 18.7, and 0 deg in each direction. At Ka-band, with a full 3-dB beamwidth of 17 mdeg, the offsets were 85, 8.5, 4.9, and 0 mdeg.

For each scan, an off-source baseline is generated from the two off-source points. A Gaussian curve (relative to the baseline) is fitted to the five remaining on-source points, and the peak value of the curve is calculated. Also, the position of the peak is calculated as a measure of the pointing error for that scan. One pair of scans (one XEL and one EL) is considered to be one measurement or data point. The seven pointing offsets for each new scan are corrected for pointing errors found from the previous similar scan, in order to maintain pointing throughout a track.

As defined here, the efficiency is referenced to the input of the low-noise amplifier (LNA) and includes the losses of the feed system. Alternative methods specify efficiency at the aperture of the feed horn or at the antenna aperture itself. The term "aperture efficiency" refers to antenna gain relative to that of a uniformly illuminated circular aperture having the same diameter as the antenna; for example, a 70-percent-efficient antenna has 1.549-dB less peak gain than does the circular aperture.

The radio-source noise-temperature increase measured by the antenna is given by [57]:

$$\Delta T = \frac{\eta S A}{2kC_r C_p} \tag{1.3-11}$$

where

η = antenna aperture efficiency

S = radio source flux (W/m^2/Hz)

A = antenna area (m^2)

k = Boltzmann constant ($1.3806503 \times 10^{-23}$ J/K)

C_r = source size correction, typically 1.0 for point sources, up to ~1.5 for extended sources, including planets

C_p = pointing correction, assumed = 1.0.

The flux, S, is typically given in units of "Janskys," where 1 Jansky (Jy) = 1×10^{-26} W/m^2/Hz.

Measured ΔT is compared with the quantity $[(SA)/(2kC_r)]$ to give antenna efficiency. Thus,

$$\eta = \frac{\Delta T}{SA/2kC_r} = \frac{\Delta T}{T_{100}/C_r} \tag{1.3-12}$$

The value T_{100} is what would be measured by a perfect antenna looking at a point source emitting the same flux as the observed radio source. The value of C_r is a function of the source structure at a given frequency and the pattern of the antenna at that frequency. For a given antenna, frequency, and radio source, the T_{100}/C_r can thus be specified.

The ΔT is an on–off source measurement, and Earth's atmosphere attenuates the true source contribution that would be measured under vacuum conditions. The total atmospheric attenuation is estimated from surface weather conditions during all measurements. The surface temperature, pressure, and relative humidity at the site are recorded every half hour. Typical zenith values of attenuation at Goldstone under average clear-sky conditions are:

X-band: $A_{zen} = 0.035$ dB

Ka-Band: $A_{zen} = 0.115$ dB

The attenuation in decibels at elevation angle, θ, is modeled as:

$$A(\theta) = \frac{A_{zen}}{\sin\theta} \tag{1.3-13}$$

The loss factor at that elevation angle is:

$$L(\theta) = 10^{A(\theta)/10} \tag{1.3-14}$$

The "vacuum ΔT" then becomes:

$$\Delta T = L(\theta)\Delta T \text{ measured} \tag{1.3-15}$$

1.3.4 Noise-Temperature Measurements

There are a variety of noise-temperature measurement techniques and instruments used in the DSN. Some of the instruments are a total power radiometer, a noise-adding radiometer, thermal noise standards (cryogenically cooled, ambient, and hot), all well described in [58]. These instruments typically calibrate low-noise systems by injecting a known amount of noise from either a gas tube or solid-state noise diode into the input. The system output power ratio is then used to calculate the operating noise temperature. It can be difficult to determine the equivalent noise temperature of the noise source, as defined at the receive input, because of component and transmission line loss between the noise source and the receiver. The calibration involves either evaluating the noise source and loss separately or calibrating the excess noise temperature directly at the receiver input.

However, a measurement technique that eliminates this problem and that is most often used for the low-noise (<<300 K) receiving systems in the DSN is the ambient termination technique [59]. The operating-noise-temperature calibrations are performed by alternately connecting the LNA input with a waveguide switch between the antenna and an ambient termination. The same effect is accomplished by alternately placing and removing an absorber load over the front of the feed horn.

The operating noise temperature of a receiving system can be expressed as

$$T_{op} = T_a + T_e \tag{1.3-16}$$

where

T_a = antenna temperature (K)

T_e = receiver effective noise temperature (K).

Figure 1-29 shows a simplified block diagram of the instrumentation for operating noise-temperature calibrations. The precision attenuator is adjusted for equal output power when the receiver input is alternately connected to the ambient load and the antenna. The power ratio for an individual measurement is

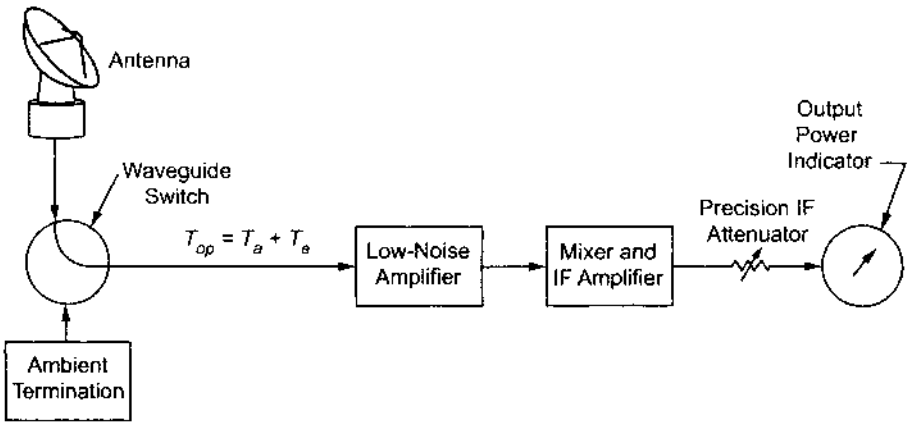

Fig. 1-29. Simplified block diagram of the operating-noise-temperature calibration instrumentation.

$$Y_{ap}(i) = \frac{T_p + T_e}{T_{op}(i)} \tag{1.3-17}$$

where

T_p = ambient termination physical temperature (K)

T_e = receiver effective noise temperature (K)

$T_{op}(i)$ = individual operating noise-temperature measurement (on antenna) (K).

Rearranging Eq. (1.3-17) gives

$$T_{op}(i) = \frac{T_p + T_e}{Y_{ap}(i)} \tag{1.3-18}$$

A series of measurements is made, and a best estimate in a least-squares sense of Y_{ap} is obtained.

The operating noise temperature is then given by

$$T_{op} = \frac{T_p + T_e}{Y_{ap}} \tag{1.3-19}$$

The ambient termination temperature is measured, and the receiver temperature is estimated or calibrated. It is not necessary to know T_e accurately if $T_e << T_p$.

In the past, the waveguide-beyond-cutoff attenuator was the most accurate instrument to measure Y-factors. Consequently, the equations were written in

terms of Y-factors. Most recently, however, the power meter has been more accurate and convenient; in addition, it mates easily with computers. Measurements in [60,61] do not use Y-factors but deal directly with power meter readings, in watts.

1.4 Techniques for Designing Beam-Waveguide Systems

A BWG feed system is composed of one or more feed horns with a series of flat and curved mirrors arranged so that power can be propagated from the feed horn, through the mirrors to the subreflector and main reflector, with minimum losses.

Feeding a large low-noise ground antenna via a BWG system has several advantages over placing the feed directly at the focal point of a dual-reflector antenna. For example, significant simplifications are possible in the design of high-power, water-cooled transmitters and low-noise cryogenic amplifiers. The feed horns do not have to rotate, a normally fed dual reflector does. For this reason, feed horns and other equipment can be located in a large, stable enclosure at an accessible location. Also, since BWG systems can transmit power over considerable distances at very low losses, they are useful in the design of very-high-frequency feed systems.

Since 1991, when the then-new DSS-13 R&D antenna was designed and constructed, the DSN has made extensive use of BWG feed systems. Various systems [62] have been designed using Gaussian-beam analysis, GO, and PO. In addition, more recently, a new technique based on a conjugate-phase-matching focal-plane method has been used. This section will outline each technique, discuss its advantages and disadvantages, and indicate where in the DSN it has been used.

Many existing BWG systems use a quasioptical design, based on Gaussian-wave principles, which optimize performance over an intended operating-frequency range. This type of design can be made to work well with relatively small reflectors (a very few tens of wavelengths) and may be viewed as "bandpass," since performance suffers as the waveglength becomes very short as well as very long. The long-wavelength end is naturally limited by the approaching small D/λ of the individual BWG reflectors used; the short-wavelength end does not produce the proper focusing needed to image the feed at the dual-reflector focus. In contrast, a purely GO design has no upper frequency limit, but performance suffers at long wavelengths. Such a design may be viewed as "highpass." The design for DSS-13 (see Chapter 7 of this monograph) was based upon a highpass design while the design for operational BWG antennas (see Chapter 8) was based on a bandpass design.

If there is a need to add frequencies to an existing BWG design outside of the original design criteria, it is sometimes difficult to generate a new solution by a straightforward analysis because of the large number of scattering surfaces required for computation. A unique application of the conjugate phase-matching technique that simplifies the design process is described in Chapter 7, which presents an example of incorporating a low-frequency S-band system into the "highpass" BWG system.

Most BWG systems refocus energy at some point along the path, but this may not be desired in high-power applications. A design technique using PO, described below, does not degrade either the peak or average power handling capability beyond the limitations imposed by either the feed or the dual reflector configuration. The Antenna Research System Task (ARST) antenna (see Chapter 9) was designed for high-power applications.

1.4.1 Highpass Design

The design for the highpass BWG system is based on GO criteria introduced by Mizusawa and Kituregawa [63,64], which guarantee a perfect image from a reflector pair. Mizusawa's criteria can be briefly stated as follows: For a circularly symmetric input beam, the conditions on a conic reflector pair necessary to produce an identical output beam are that

- The four loci (two of which may be coincident) associated with the two curved reflectors must be arranged on a straight line
- The eccentricity of the second reflector must be equal to the eccentricity or the reciprocal of the eccentricity of the first reflector.

Figure 1-30 shows some curved reflector pair orientations that satisfy Mizusawa's criteria.

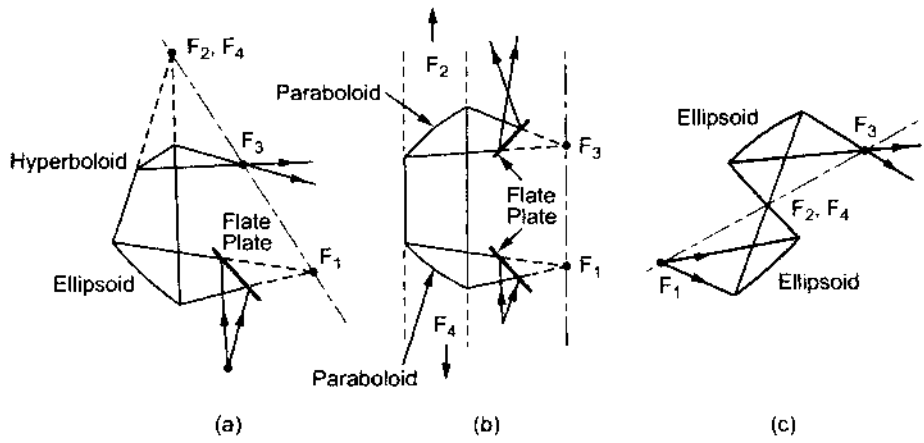

Fig. 1-30. Examples of two curved-reflector BWG configurations.

This technique was used for the first DSN BWG antenna (DSS-13), the design of which is shown and described in detail in Chapter 7 of this monograph. The design of DSS-13's center-fed BWG consists of a beam-magnifier ellipse in a pedestal room located below ground level that transforms a 22-dB gain feed horn into a high-gain 29-dB pattern for input to a Mizusawa four-mirror (two flat and two paraboloid-case) BWG system [see Fig. 1-30(b) and 1-31]. The system was initially designed for operation at 8.45 GHz (X-band) and 32 GHz (Ka-band) and loses fewer than 0.2 dB at X-band (determined by

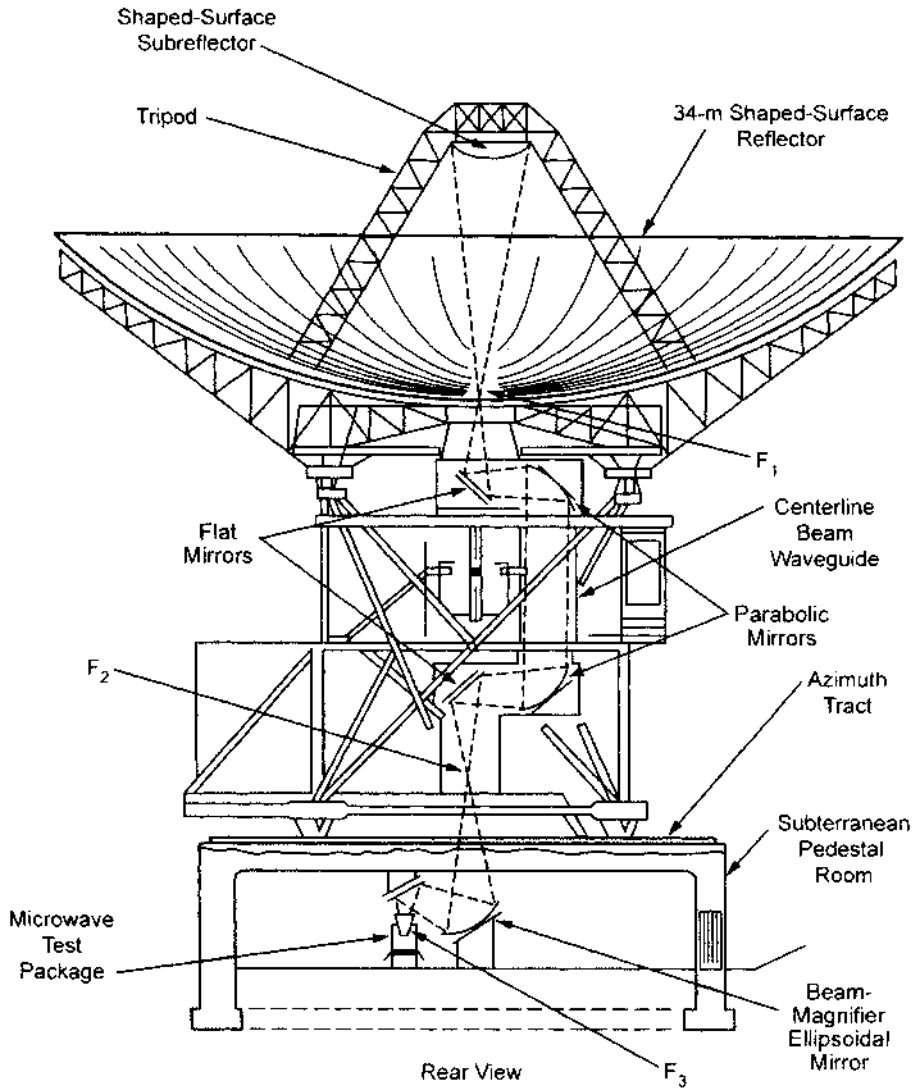

Fig. 1-31. DSS-13 highpass BWG design.

comparing the gain of a 29-dB gain horn feeding the dual-shaped reflector system with that obtained using the BWG system).

Since the upper BWG has an 8-ft (2.44-m)-diameter projected aperture, the mirrors are 70 wavelengths at X-band and 260 wavelengths at Ka-band. These mirrors are large enough to use GO design criteria.

Even though the design was based upon GO, all performance analysis was done using PO computer programs.

1.4.2 Focal-Plane Matching

The DSS-13 BWG system was initially designed (see Chapter 7 of this monograph for details of Phase I) for operation at X-band (8.45 GHz) and Ka-band (32 GHz) and utilized a GO design technique. The addition of S-band (2.025–2.120 GHz transmit and 2.2–2.3 GHz receive) was scheduled for a later phase. (At S-band, the mirror diameter is only 19 wavelengths, clearly outside the original GO design criteria.)

If a standard JPL 22-dB S-band feed horn is placed at the input focus of the ellipse, the BWG loss is greater than 1.5 dB. This is primarily because for low frequencies, the diffraction phase centers are far from the GO mirror focus, resulting in a substantial spillover and defocusing loss. The defocusing is especially a problem for the beam-magnifier ellipse, where the S-band phase center at the output of the ellipse is three meters from the GO focus.

A potential solution is to redesign the feed horn to provide an optimum solution for S-band. The question is how to determine the appropriate gain and location for this feed.

A straightforward design by analysis would prove cumbersome because of the large number of scattering surfaces required for the computation. Therefore, a unique application was made of the conjugate phase-matching techniques to obtain the desired solution [65]. Specifically, a plane wave was used to illuminate the main reflector and the fields from the currents induced on the subreflector propagated through the BWG to a plane centered on the input focal point. By taking the complex conjugate of the currents induced on the plane and applying the radiation integral, the far-field pattern was obtained for a theoretical feed horn that maximized antenna gain.

There is no a priori guarantee that the patterns produced by this method will be easily realized by a practical feed horn. However, for DSS-13, the pattern was nearly circularly symmetrical, and the theoretical horn was matched fairly well by a circular corrugated horn.

The corrugated feed-horn performance was only 0.22 dB lower than that of the optimum theoretical horn and about 1.4 dB better than by using the 22-dB feed horn. Subsequently, a system employing the corrugated feed horn was built, tested, and installed in the DSS-13 34-m BWG antenna as part of a simultaneous S-/X-band receiving system [66].

1.4.3 Gaussian-Beam Design

While GO is useful for designing systems with electrically large mirrors (>50-wavelength diameter with –20-dB edge taper), some BWGs may be operated at low frequencies, where the mirrors may be as small as 20 wavelengths in diameter. Due to diffraction effects, the characteristics of a field propagated between small BWG mirrors (<30 wavelengths in diameter) will be substantially different from those resulting from the GO solution. For these cases, the Gaussian-beam technique is used.

Solutions to the paraxial wave equation are Gaussian-beam modes. These solutions describe a beam that is unguided but effectively confined near an axis. The zero-order mode is normally used in the design. A major advantage of applying the Gaussian-beam technique is the simplicity of the Gaussian formula, which is easy to implement and requires negligible computation time. Because of the negligible computation time, a Gaussian solution can be incorporated with an optimization routine to provide a convenient method to search the design parameters for a specified frequency range, mirror sizes and locations, and feed-horn parameters.

Goubau [67] gave the first mathematical expression of Gaussian modes derived from the solution of Maxwell's equations described by a continuous spectrum of cylindrical waves. Chu [68] developed the Fresnel zone imaging principle of the Gaussian beam to design a pseudo frequency-independent BWG feed. Betsudan, Katagi, and Urasaki [69] used a similar imaging technique to design large ground-based BWG antennas. McEwan and Goldsmith [70] developed a simple design procedure based on the Gaussian-beam theory for illumination of reflector antennas where the reflector is electrically small or in the near field of a feed.

Although Gaussian-beam analysis is fast and simple, it is less accurate than the PO solution for smaller mirrors (<30 wavelengths in diameter). However, by designing with Gaussian-beam analysis, then checking and adjusting using PO analysis, an accurate and efficient tool can be fashioned. Veruttipong [71] developed such a tool for designing a second 34-m BWG antenna for the DSN. The goal was to provide good performance over the range of 2 to 32 GHz. (As demonstrated by design and measurements, the use of the GO technique in conjunction with the focal-plane-matching technique produced an antenna with virtually the same characteristics as the antenna designed using Gaussian-beam analysis [see Chapters 7 and 8].)

The design of this antenna is similar to that of DSS-13 (see Fig. 1-31) in that it uses three curved mirrors (one in the basement room and two rotating in azimuth) and a 34-m dual-shaped reflector antenna (Fig. 1-32). Multiple-frequency operation is provided by the use of dichroic mirrors. The desire is to have the radius of curvature and –18-dB beam diameter of the Gaussian beam

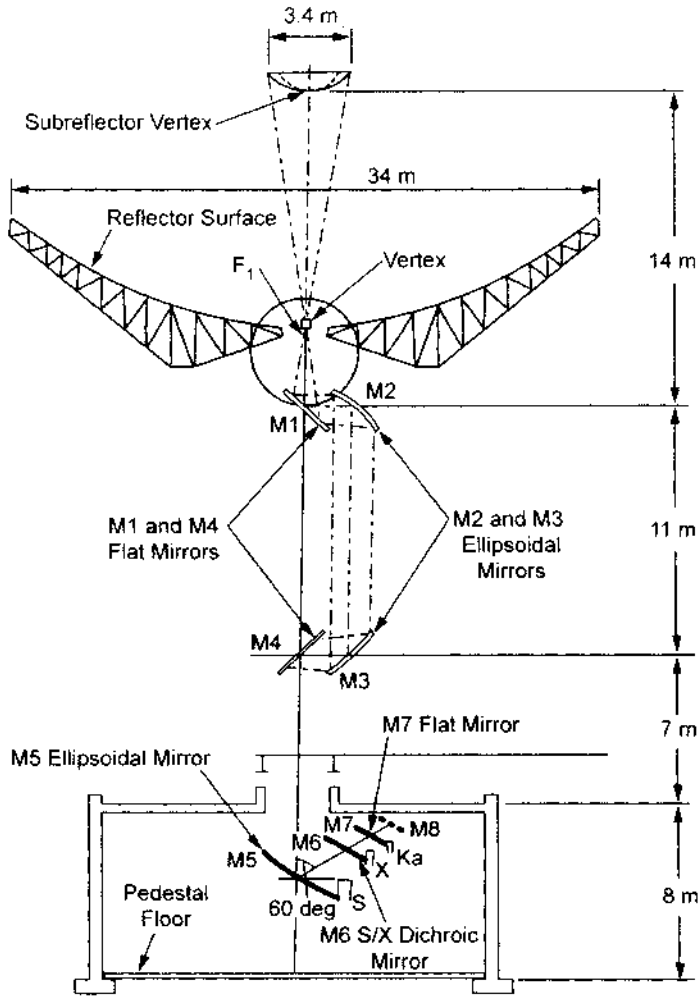

Fig. 1-32. Operational BWG antenna.

at the subreflector be the same at all frequencies. The size and locations of the mirrors are relatively fixed because of the basic structure geometry, so the pertinent variables are the feed-horn diameters, horn positions, and mirror curvatures. Approximating the mirrors by a thin-lens formula (Fig. 1-33) and using Gaussian-mode analysis to iterate the various design parameters, a design is achieved that meets the initial design constraint of identical patterns at the subreflector. Using the technique described above, a 34-m BWG antenna was built and measured at S-, X-, and Ka-bands (see Chapter 8 for details).

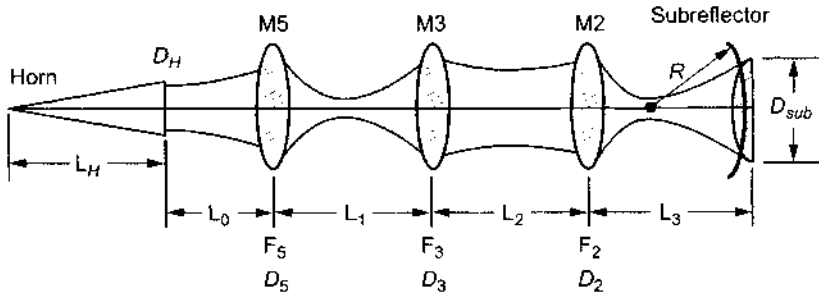

Fig. 1-33. Parameters for BWG Gaussian design.

1.4.4 High-Power Design

Observe that the GO technique used to design the BWG system images (refocuses) the feed horn at a location near the main reflector (position F_1 in Fig. 1-31).

The refocusing of the feed system energy near the main reflector has two distinct disadvantages. For one, although the phase center is inside the feed, the peak field point is generally at or in front of the feed itself. Thus, this peak power point is imaged in front of the main reflector. If the peak field point can be contained within the BWG system, there is the possibility to fill the BWG tube with a gas to enhance the peak power-handling capability of the system. Also, when energy is reflected from a surface such as a BWG mirror, there is a 6-dB enhancement of the power near the reflector, since the incident and reflector field add coherently near the reflection point.

It is thus important to have the energy near the mirrors at least 6 dB below the peak point in order to prevent the mirrors from degrading the power-handling capability of the system. This is difficult to do if the energy is refocused in the BWG system. For these reasons, an unconventional design required for the BWG optics. Figure 1-34 shows the geometry of optics for the high-power design antenna ([72] and Chapter 9).

For this design, only one curved mirror—a paraboloid—is used, along with three flat mirrors. The radiation from the feed horn is allowed to spread to the paraboloid, where it is focused to a point at infinity. That is, after reflection, a collimated beam exists that is directed to the subreflector by the three flat reflectors. The energy is thus spread over the entire 9-ft (2.74-m) diameter of the BWG tube. The beam reflected by the paraboloid does not begin to spread significantly due to diffraction until it exists through the main reflector. Additional spreading occurs in the region between the main reflector and the subreflector. Since a collimated beam exists beyond the first mirror, the design of this antenna is closely related to a near-field Cassegrain design, if the feed sys-

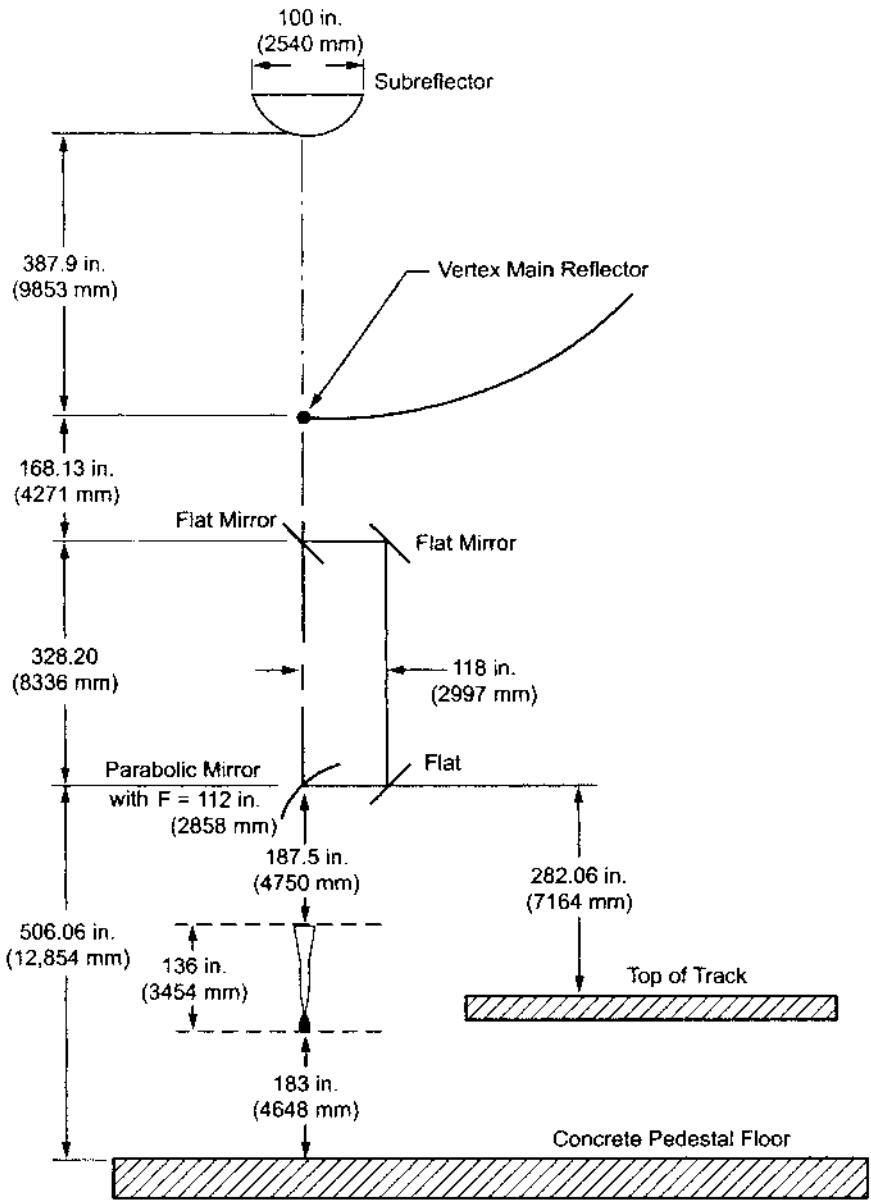

Fig. 1-34. Design for a high-power BWG.

tem is defined to include both the feed horn and a parabolic mirror. The main reflector and subreflector are then determined through a standard symmetric uniform aperture synthesis program using the PO-determined input pattern radiated from the feed and four mirrors. Design and performance are described in detail in Chapter 9.

1.5 Summary

Since it is usually impractical to build a scale-model antenna to test new designs, accurate analytical techniques are required. These analytical techniques have evolved to the point where they can reliably and accurately predict the performance of a new design, thus eliminating the need for trial and error. The measurement techniques that have been developed can accurately characterize the performance of the antennas.

The remainder of this monograph describes in detail the RF design and performance of the large antennas of the DSN and illustrates the use of these techniques. Included are comparisons made between the predicted and measured performance of the antennas.

References

[1] R. F. Harrington, *Time-Harmonic Electromagnetic Fields*, New York: McGraw-Hill, 1961.

[2] W. V. T. Rusch and P. D. Potter, *Analysis of Reflector Antennas*, New York: Academic Press, 1970.

[3] W. A. Imbriale and R. E. Hodges, "Linear-Phase Approximation in the Triangular Facet Near-Field Physical Optics Computer Program," *Telecommunications and Data Acquisition Progress Report 42-102*, vol. April–June 1990, http://tmo.jpl.nasa.gov/progress_report/issues.html Accessed December 2001.

[4] W. A. Imbriale and R. E. Hodges, "The Linear Phase Triangular Facet Approximation in Physical Optics Analysis of Reflector Antennas," *Applied Computational Electromagnetic Society*, vol. 6, no. 2, pp. 74–85, Winter 1991.

[5] A. W. Rudge, K. Milne, A. D. Olver, and P. Knight, *The Handbook of Antenna Design, Volumes 1 and 2*, London: Peter Peregrinus, 1982.

[6] S. W. Lee and R. Mittra, "Fourier Transform of a Polygonal Shape Function and Its Application in Electromagnetics," *IEEE Transactions on Antennas and Propagation*, vol. 31, no. 1, pp. 99–103, January 1983.

[7] Y. Rahmat-Samii, "Useful Coordinate Transformations for Antenna Applications," *IEEE Transactions on Antennas and Propagation*, vol. 27, pp. 571–574, July 1979.

[8] J. R. Withington, W. A. Imbriale, and P. Withington, "The JPL Beam-waveguide Test Facility," Antennas and Propagation Society Symposium, London, Ontario, Canada, pp. 1194–1197, June 24–28, 1991.

[9] P. D. Potter, A new horn antenna with suppressed sidelobes and equal beamwidths, *Microwave Journal*, pp. 71–78, June 1963.

[10] S. A. Brunstein, "A New Wideband Feed Horn with Equal E- and H-plane Beamwidths and Suppressed Sidelobes," *Space Programs Summary 37-58, Vol. II, The Deep Space Network*, Jet Propulsion Laboratory, Pasadena, California, pp. 61–64, July 1969.

[11] D. Hoppe, "Scattering Matrix Program for Circular Waveguide Junctions," *Cosmic Software Catalog*, NASA-CR-179669, NTO-17245, National Aeronautics and Space Administration, Washington, D.C., 1987.

[12] D. Hoppe, "Modal Analysis Applied to Circular, Rectangular and Coaxial Waveguides," *Telecommunications and Data Acquisition Progress Report 42-95*, vol. July–September 1988, http://tmo.jpl.nasa.gov/progress_report/issues.html Accessed December 2001.

[13] D. Hoppe, W. Imbriale, and A. Bhanji, "The Effects of Mode Impurity on Ka-band System Performance," *Telecommunications and Data Acquisition Progress Report 42-80*, vol. October–December 1984, http://tmo.jpl.nasa.gov/progress_report/issues.html Accessed December 2001.

[14] G. L. James, "Analysis and Design of TE_{11} and HE_{11}, Corrugated Cylindrical Waveguide Mode Converters," *IEEE Transactions on Microwave Theory and Techniques*, vol. MTT-29, pp. 1059–1066, October 1981.

[15] A. C. Ludwig, "Radiation Pattern Synthesis for Circular Aperture Horn Antennas," *IEEE Transactions on Antennas and Propagation*," vol. AP-14, pp. 434–440, July 1966.

[16] S. Silver, *Microwave Antenna Theory and Design*, Radiation Laboratory Series, vol. 12, New York: McGraw-Hill, pp. 336–338, 1949.

[17] P. H. Stanton, D. J. Hoppe, H. Reilly, "Development of a 7.2-, 8.4-, and 32-Gigahertz (X-/X-/Ka-Band) Three-Frequency Feed for the Deep Space Network," *Telecommunications and Mission Operations Progress Report 42-145*, vol. January–March 1991, http://tmo.jpl.nasa.gov/progress_report/issues.html Accessed December 2001.

[18] A. C. Ludwig, "Spherical Wave Theory," section in *Handbook of Antenna Design* (A. W. Rudge, et al., editors), London: Peter Peregrinus, 1982.

[19] A. C. Ludwig, *Calculation of Scattered Patterns from Asymmetrical Reflectors*, Ph.D. dissertation, University of Southern California, Los

Angeles, 1969. Also *Technical Report 32-1430,* Jet Propulsion Laboratory, Pasadena, California, February 1970.

[20] V. Galindo, "Design of Dual-Reflector Antennas with Arbitrary Phase and Amplitude Distributions," *IEEE Transactions on Antennas and Propagation*, vol. AP-12, pp. 403–408, July 1964.

[21] W. F. Williams, "High Efficiency Antenna Reflector," *Microwave Journal*, vol. 8, pp. 79–82, July 1966.

[22] V. Galindo-Israel, W. A. Imbriale, and R. Mittra, "On the Theory and Synthesis of Single and Dual Offset Shaped Reflector Antennas," *IEEE Transactions on Antennas and Propagation*, vol. AP-35, no. 8, pp. 887–896, August 1987.

[23] V. Galindo-Israel, W. A. Imbriale, R. Mittra, and K. Shogen, "On the Theory of the Synthesis of Offset Dual-Shaped Reflectors—Case Examples," *IEEE Transactions on Antennas and Propagation*, vol. 39, no. 5, pp. 620–626, May 1991.

[24] A. G. Cha, "The JPL 1.5-meter Clear Aperture Antenna with 84.5 Percent Efficiency," *Telecommunications and Data Acquisition Progress Report 42-73*, vol. January–March 1983, http://tmo.jpl.nasa.gov/progress_report/issues.html Accessed December 2001.

[25] W. A. Imbriale and D. J. Hoppe, "Computational Techniques for Beam Waveguide Systems," *2000 IEEE Antennas and Propagation International Symposium*, Salt Lake City, Utah, pp. 1894–1897, July 16–21, 2000.

[26] W. A. Imbriale and D. J. Hoppe, "Recent Trends in the Analysis of Quasioptical System," AP2000 Millennium Conference on Antennas and Propagation, Davos, Switzerland, April 9–14, 2000.

[27] P. F. Goldsmith, *Quasioptical Systems*, New York: IEEE Press, pp. 26–29, 1998.

[28] C. C. Chen, "Transmission of Microwave Through Perforated Flat Plates of Finite Thickness," *IEEE Transactions on Microwave Theory and Techniques*, vol. MTT-21, no. 1, pp. 1–6, January 1973.

[29] J. C. Chen "Analysis of a Thick Dichroic Plate with Rectangular Holes at Arbitrary Angles of Incidence," *Telecommunications and Data Acquisition Progress Report 42-104,* vol. October–December 1990, http://tmo.jpl.nasa.gov/progress_report/issues.html Accessed December 2001.

[30] W. A. Imbriale, "Analysis of a Thick Dichroic Plate with Arbitrarily Shaped Holes," *InterPlanetary Network Progress Report 42-146*, vol. April–June 2001, http://tmo.jpl.nasa.gov/progress_report/issues.html Accessed December 2001.

[31] V. D. Agrawal and W. A. Imbriale, "Design of a Dichroic Cassegrain Subreflector," *IEEE Transactions on Antennas and Propagation*, vol. AP-27, no. 4, pp. 466–473, July 1979.

[32] J. P. Montgomery, "Scattering by an Infinite Periodic Array of the Conductors on a Dielectric Sheet," *IEEE Transactions on Antennas and Propagation*, vol. AP-23, no. 1, pp. 70–75, January 1975.

[33] R. Silvester, "Finite-element Solution of Homogeneous Waveguide Problems," *Alta Frequenza*, vol. 38, pp. 313–317, 1969.

[34] J. C. Chen, P. H. Stanton, and H. F. Reilly, "Performance of the X-/Ka-/KABLE-Band Dichroic Plate in the DSS-13 Beam Waveguide Antenna," *Telecommunications and Data Acquisitions Progress Report 42-115*, vol. July–September 1991, http://tmo.jpl.nasa.gov/progress_report/issues.html Accessed December 2001.

[35] W. Veruttipong and M. Franco, "A Technique for Computation of Noise Temperature Due to a Beam Waveguide Shroud," *1993 IEEE International Antennas and Propagation Symposium Digest*, The University of Michigan at Ann Arbor, pp. 1659–1662, June 28–July 2, 1993.

[36] A. G. Cha and W. A. Imbriale, "A New Analysis of Beam Waveguide Antennas Considering the Presence of the Metal Enclosure," *IEEE Transactions on Antennas and Propagation*, vol. 40, no. 9, pp. 1041–1046, September 1992.

[37] W. A. Imbriale, "On the Calculation of Noise Temperature in Beam Waveguide Systems," *Proceedings of the International Symposium on Antennas and Propagation*, Chiba, Japan, pp. 77–80, September 24–27, 1996.

[38] W. Imbriale, W. Veruttipong, T. Otoshi, and M. Franco, "Determining Noise Temperature in Beam Waveguide Systems," *Telecommunications and Data Acquisition Progress Report 42-116*, vol. October–December 1993, http://tmo.jpl.nasa.gov/progress_report/issues.html Accessed December 2001.

[39] W. A. Imbriale, T. Y. Otoshi, and C. Yeh, "Power Loss for Multimode Waveguide and Its Application to Beam-Waveguide Systems," *IEEE Transaction on Microwave Theory and Techniques*, vol. 46, no. 5, pp. 523–529, May 1998.

[40] R. F. Harrington, *Time-Harmonic Electromagnetic Fields*, New York: McGraw-Hill, pp. 381–391, 1961.

[41] D. A. Bathker, W. Veruttipong, T. Y. Otoshi, and P. W. Cramer, Jr., "Beam Waveguide Antenna Performance Predictions with Comparisons

to Experimental Results," *Microwave Theory and Techniques, Special Issue (Microwaves in Space)*, vol. MTT-40, no. 6, pp. 1274–1285, 1992.

[42] R. Levy, "Structural Engineering of Microwave Antennas," New York: IEEE Press, pp. 289–296, 1996.

[43] R. Levy, "DSS-13 Antenna Structure Measurements and Evaluation," JPL D-8947 (internal document), Jet Propulsion Laboratory, Pasadena, California, October 1, 1991.

[44] M. Brenner, M. J. Britcliffe, W.A. Imbriale, "Gravity Deformation Measurements of 70m Reflector Surfaces," Antenna Measurement Techniques Association 2001 Conference, Denver, Colorado, October 21–26, 2001.

[45] J. Ruze, "Antenna Tolerance Theory—A Review," *Proceedings of the IEEE*, vol. 54, pp. 633–640, 1966.

[46] D. J. Rochblatt and B. L. Seidel, "DSN Microwave Antenna Holography," *Telecommunications and Data Acquisition Progress Report 42-76*, vol. October–December 1983, http://tmo.jpl.nasa.gov/progress_report/issues.html Accessed December 2001.

[47] D. J. Rochblatt, "A Microwave Holography Methodology for Diagnostics and Performance Improvement for Large Reflector Antennas," *Telecommunications and Data Acquisition Progress Report 42-108*, October–December 1991, http://tmo.jpl.nasa.gov/progress_report/issues.html Accessed December 2001.

[48] D. J. Rochblatt and B. L. Seidel, "Performance Improvement of DSS-13 34-meter Beam-Waveguide Antenna Using the JPL Microwave Methodology," *Telecommunications and Data Acquisition Progress Report 42-108*, vol. October–December 1991, http://tmo.jpl.nasa.gov/progress_report/issues.html Accessed December 2001.

[49] D. J. Rochblatt, "System Analysis for DSN Microwave Antenna Holography," *Telecommunications and Data Acquisition Progress Report 42-97*, vol. January–March 1989, http://tmo.jpl.nasa.gov/progress_report/issues.html Accessed December 2001.

[50] D. J. Rochblatt and Y. Rahmat-Samii, "Effects of Measurement Errors on Microwave Antenna Holography," *IEEE Transactions on Antennas and Propagation*, vol. 39, no. 7, pp. 933–942, July 1991.

[51] Y. Rahmat-Samii, "Surface Diagnosis of Large Reflector Antennas Using Microwave Metrology—An Iterative Approach," *Radio Science*, vol. 19, no. 5, pp. 1205–1217, September–October 1984.

[52] M. J. Britcliffe, L. S. Alvarez, D. A. Bathker, P. W. Cramer, T. Y. Otoshi, D. J. Rochblatt, B. L. Seidel, S. D. Slobin, S. R. Stewart, W. Veruttipong,

and G. E. Wood, "DSS 13 Beam Waveguide Atnenna Project: Phase 1 Final Report," JPL D-8451 (internal document), Jet Propulsion Laboratory, Pasadena, California, May 15, 1991.

[53] S. D. Slobin, T. Y. Otoshi, M. J. Britcliffe, L. S. Alvarez, S. R. Stewart, and M. M. Franco, "Efficiency Calibration of the DSS 13 34-meter Beam-Waveguide Antenna at 8.45 and 32 GHz," *Telecommunications and Data Acquisition Progress Report 42-106*, vol. April–June 1991, http://tmo.jpl.nasa.gov/progress_report/issues.html Accessed December 2001.

[54] L. S. Alvarez, "Analysis and Applications of a General Boresight Algorithm for the DSS 13 Beam-Waveguide Antenna," *Telecommunications and Data Acquisition Progress Report 42-111*, vol. July–September 1992, http://tmo.jpl.nasa.gov/progress_report/issues.html Accessed December 2001.

[55] P. H. Richter and S. D. Slobin, "DSN 70-meter Antenna X- and S-band Calibration Part I: Gain Measurements," *Telecommunications and Data Acquisition Progress Report 42-97*, vol. January–March 1989, http://tmo.jpl.nasa.gov/progress_report/issues.html Accessed December 2001.

[56] P. Richter, "DSN Radio Source List for Antenna Calibration," JPL D-3801, Rev. C (internal document), Jet Propulsion Laboratory, Pasadena, California, August 19, 1993.

[57] J. A. Turegano and M. J. Klein, "Calibration Radio Sources for Radio Astronomy: Precision Flux Density Measurements at 8420 MHz," *Astronomy and Astrophysics*, vol. 86, pp. 46–49, 1980.

[58] C. Stelzried, "The Deep Space Network—Noise Temperature Concepts, Measurements, and Performance," JPL Publication 82-33, Jet Propulsion Laboratory, Pasadena, California, September 15, 1982.

[59] C. T. Stelzried, "Operating Noise-Temperature Calibrations of Low-Noise Receiving Systems," *Microwave Journal*, vol. 14, no. 6, p. 41–48, June 1971.

[60] C. T. Stelzried and M. J. Klein, "Precision DSN Radiometer Systems: Impact on Microwave Calibrations," *Proceedings of the IEEE*, vol. 82, no. 5, pp. 776–787, May 1994.

[61] C. T. Stelzried and M. J. Klein, corrections to "Precision DSN Radiometer Systems: Impact on Microwave Calibrations," *Proceedings of the IEEE*, vol. 84, no. 8, p. 1187, August 1996.

[62] W. A. Imbriale, "Design and Applications of Beam Waveguide Systems," *1997 IEEE Aerospace Conference*, vol. 3, Snowmass, Colorado, pp. 121–134, February 1–8, 1997.

[63] M. Mizusawa and T. Kitsuregawa, "A Beam-waveguide Feed Having a Symmetric Beam for Cassegrain Antennas," *IEEE Transactions on Antennas and Propagation*, vol. AP-21, no. 6, pp. 844–846, November 1973.

[64] T. Veruttipong, J. R. Withington, V. Galindo-Israel, W. A. Imbriale, and D. Bathker, "Design Considerations for Beam-waveguide in the NASA Deep Space Network," *IEEE Transactions on Antennas and Propagation*, vol. AP-36, no. 12, pp. 1779–1787, December 1988.

[65] W. A. Imbriale and J. S. Esquival, "A Novel Design Technique for Beam-waveguide Antennas," *1996 IEEE Aerospace Applications Conference Proceedings*, vol. 1, Aspen, Colorado, pp. 111–127, February 3–10, 1996.

[66] W. A. Imbriale, M. S. Esquivel, and F. Manshadi, "Novel Solutions to Low-frequency Probelms with Geometrically Designed Beam-waveguide systems," *IEEE Transactions on Antennas and Propagation*, vol. 46, no. 12, pp. 1790–1796, December 1998.

[67] G. Goubau and F. Schwering, "On the Guide Propagation of Electromagnetic Wave Beams," *Institute of Radio Engineers Transactions on Antennas and Propagation*, vol. AP-9, no. 5, pp. 248–256, May 1961.

[68] T. S. Chu, "An Imaging Beam Waveguide Feed," *IEEE Transactions on Antennas Propagation*, vol. AP-31, no. 4, pp. 614–619, July 1983.

[69] S. Betsudan, T. Katagi, and S. Urasaki, "Design Method of Four Reflector-Type Beam Waveguide Feeds," *Japanese Electronics and Communications Society Journal*, vol. J67-B, no. 6, pp. 622–629, June 1984.

[70] N. J. McEwan and P. F. Goldsmith, "Gaussian Beam Techniques for Illuminating Reflector Antenna," *IEEE Transactions on Antennas and Propagation*, vol. 37, no. 3, pp. 297–304, March 1989.

[71] W. Veruttiong, J. C. Chen, and D. A. Bathker, "Gaussian Beam and Physical Optics Iteration Technique for Wideband Beam Waveguide Feed Design," *Telecommunications and Data Acquisition Progress Report 42-105*, vol. January–March 1991, http://tmo.jpl.nasa.gov/progress_report/issues.html Accessed December 2001.

[72] W. A. Imbriale, D. J. Hoppe, M. S. Esquivel, and B. L. Conroy, "A Beamwaveguide Design for High-Power Applications," *Intense Microwave and Particle Beams III*, proceedings of the SPIE meeting, Los Angeles, California, pp. 310–318, January 20–24, 1992.